RIGA TECHNICAL UNIVERSITY

Vsevolod Burenin

RESEARCH, DEVELOPMENT, AND EVALUATION OF A CONTROL SYSTEM FOR ELECTRIC TRACTION DRIVES IN RAILWAY APPLICATIONS

Summary of the Doctoral Thesis

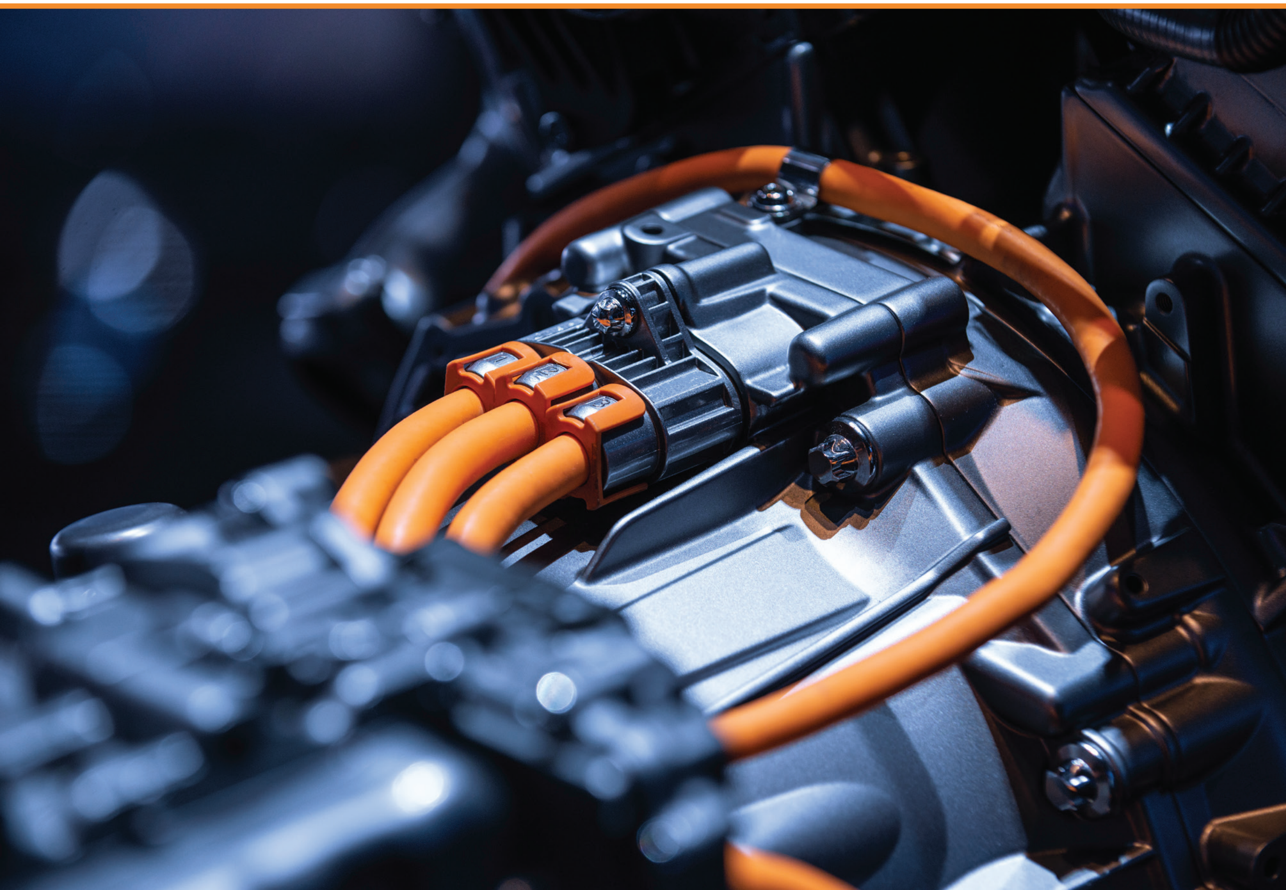

RTU Press
Riga 2025

RIGA TECHNICAL UNIVERSITY
Faculty of Computer Science, Information Technology and Energy
Institute of Industrial Electronics, Electrical Engineering and Energy

Vsevolod Burenin
Doctoral Student of the Study Programme "Computerized Control of Electrical Technologies"

RESEARCH, DEVELOPMENT, AND EVALUATION OF A CONTROL SYSTEM FOR ELECTRIC TRACTION DRIVES IN RAILWAY APPLICATIONS

Summary of the Doctoral Thesis

Scientific supervisor
Professor Dr. sc. ing. OSKARS KRIEVS

RTU Press
Riga 2025

Burenin, V. Research, Development, and Evaluation of a Control System for Electric Traction Drives in Railway Applications. Summary of the Doctoral Thesis. – Riga: RTU Press, 2025. – 62 p.

Published in accordance with the decision of the Promotion Council "RTU P-14" of 11 November 2024, Minutes No. 33800-4/2.

https://doi.org/10.7250/9789934371486
ISBN 978-9934-37-148-6 (pdf)

DOCTORAL THESIS PROPOSED TO RIGA TECHNICAL UNIVERSITY FOR PROMOTION TO THE SCIENTIFIC DEGREE OF DOCTOR OF SCIENCE

To be granted the scientific degree of Doctor of Science (Ph. D.), the present Doctoral Thesis has been submitted for defence at the open meeting of the RTU Promotion Council on February 21, 2025, at the Faculty of Computer Science, Information Technology and Energy of Riga Technical University, 12 K-1 Azenes Street, Room 306.

OFFICIAL REVIEWERS

Professor Dr. sc. ing. Nadežda Kuņicina,
Riga Technical University

Senior Researcher Ph. D. Dmitri Vinnikov,
Tallinn University of Technology, Estonia

Professor George Parafotiou,
Technical University Eindhoven, Netherlands

DECLARATION OF ACADEMIC INTEGRITY

I hereby declare that the Doctoral Thesis submitted for review to Riga Technical University for promotion to the scientific degree of Doctor of Science (Ph. D) is my own. I confirm that this Doctoral Thesis has not been submitted to any other university for promotion to a scientific degree.

Vsevolod Burenin ……………………………. (signature)

Date: ………………………

The Doctoral Thesis has been written in English. It consists of an Introduction, 4 chapters, Conclusions, 83 figures, 56 tables, and 4 appendices; the total number of pages is 169, including appendices. The Bibliography contains 108 titles.

Table of Contents

List of Abbreviations

EMU – electric multiple unit

FOC – field-oriented control

IGBT – insulated gate bipolar transistor

MPC – model predictive control

OPP – optimized pulse pattern

PPWM – pre-programmed pulse width modulation

PWM – pulse width modulation

SHE – selective harmonic elimination

SHM – selective harmonic mitigation

SPWM – sinusoidal pulse width modulation

SVPWM – space vector pulse width modulation

THD – total harmonic distortion

WTHD – weighted total harmonic distortion

General description of the Thesis

Research relevance

Railway traction electric drives are used in widely different types of electrification systems, with most of them being attributed to the high-power medium voltage category. Most of these systems are customized to specific types or series of rail transport, with traction electric motor and power converter being two of the most important components.

Traction electric motors enable the mechanical propulsion of the train. Currently, the most widely used type of motor is the squirrel cage induction motor [1], [2], [3], although there is increasing adoption of permanent magnet synchronous machines [4]. Leading producers of traction electric motors for the railway industry include TSA, ABB, Mitsubishi, Siemens, Alstom, and Škoda. In Baltic countries, Latvian factory JSC "Rīgas elektromašīnbūves rūpnīca" stands as a prominent producer of traction electric motors for trains, trams, and subways.

Power converters are another fundamental component of traction electric drives. They are used to ensure power efficiency and density, controllability and stability of electric drive operation. Power converters heavily rely on power semiconductors. Currently, insulated gate bipolar transistors (IGBTs) dominate the space of traction electric drives, utilized extensively across a spectrum of power levels from a few kilowatts to several megawatts [4]. Despite significant development and investment in silicon carbide (SiC) semiconductor technologies, SiC semiconductors for medium to high-power applications are still in the developmental phase.

Currently, the most commonly used IGBTs in the railway industry have blocking voltages of 3300 VDC [5], 4500 VDC and 6500 VDC [6], [7], with some solutions utilizing 1700 VDC [3]. SiC devices have currently proven reliability for commercial automotive use and are available in both pure SiC and hybrid configurations with a 1200 VDC blocking voltage [8], [9], [10], while the 1700 VDC variants are just entering the market. These devices are increasingly being used in light vehicle applications, such as electric cars [11], [12], [13]. The introduction of high-power applications for railways is underway, with the expectation that SiC power semiconductors with a 3300 VDC blocking voltage will start entering the market between 2026 and 2030 [10], [12], [13].

Currently, the primary producers of power IGBTs for the railway industry include ABB, Infineon, Mitsubishi Electric, Hitachi, and Fuji Electric, among others [4].

Over the years, technological advancements in the field of power semiconductors improved the controllability and stability of power semiconductors within a specific temperature range. However, switching and ON-state losses at high powers still result in excessive junction temperatures that lead to reduced service life and reliability of the device. Therefore, it is common practice to employ low switching frequencies in rail traction systems to reduce IGBT switching losses, thereby enhancing their life expectancy [14], [15]. 2-level topology, commonly used in high-power applications, typically limits the switching frequency of the converter to a range from a few hundred hertz up to 1 kHz [6], [16], [17], [18], [19], [20], whereas the 3-level topology is reported to operate up to 2 kHz [6], [21]. The choice of topology depends on various parameters, with no single option deemed universally superior.

Operating at reduced frequencies presents its own set of challenges, including increased harmonic distortion in the stator current. This is particularly undesirable as higher current harmonics can significantly increase losses in the induction motor [22], [23].

To mitigate harmonic distortion while maintaining a low switching frequency, specialized modulation techniques are employed. Since their inception, pulse width modulation (PWM) techniques have undergone rapid evolution. General PWM techniques have been extensively studied and compared for induction motor drives. These techniques aim to achieve better DC bus voltage utilization, optimize converter harmonics and losses, and enhance the output frequency spectrum of three-phase converters and other indicators [14].

There exists a multitude of PWM approaches. Commonly utilized methods include sinusoidal PWM (SPWM), space vector PWM (SVPWM) and discontinuous PWM, among others. However, there are also pre-programmed PWM techniques, such as selective harmonic elimination (SHE), selective harmonic mitigation (SHM) PWM, and optimized pulse pattern (OPP). These pre-programmed techniques are aimed at improving the current waveform at very low switching frequencies, enabling the elimination or minimization of predetermined harmonics while maintaining the fundamental current harmonic at the predefined level of the modulation index. Among these techniques, SHE stands out as the most well-known strategy [24], [25], [14], [17].

The prevailing approach to modulation in railway traction electric drives involves a combination of asynchronous and synchronous SVPWM at lower frequencies, transitioning to variations of SHE/SHM approaches, and potentially shifting to square wave modulation at higher speeds if necessary. This amalgamation of modulation techniques is referred to as a hybrid PWM.

The primary objective of this research is to develop a control system for a traction induction motor, incorporating a low switching frequency hybrid PWM. The proposed system will be rigorously tested on a downscaled laboratory prototype to assess its performance and stability, offering a comprehensive evaluation within the context of railway applications.

Aim, research methods, and novelty of the Thesis

The aim of the research

Developing and validating a control system for railway traction electric drives using a downscaled laboratory prototype based on a 2-level inverter.

Research tasks

1. Investigate control and PWM strategies applicable to railway applications.
2. Develop a modulation algorithm based on the selected PWM strategy.
3. Design the traction drive field-oriented control system, integrating the chosen PWM strategy.
4. Create and simulate an electric drive model to analyse expected operational regimes.
5. Develop a testing setup for the control system.
6. Conduct tests on the control system using a 2-level inverter in a downscaled laboratory setup.
7. Analyse and evaluate the results of laboratory testing.

Research tools and methods

- MATLAB was used in this study for the calculation of SHE-PWM solutions. It played a vital role in processing recorded data, conducting thorough data analysis, and creating visualizations to support the findings.
- Simulink was used for the creation and simulation of the electrical drive model. Both built-in library blocks and custom-developed MATLAB functions were used in a Simulink model.
- MS Excel was used as a storage for traction characteristic reference and equivalent circuit reference as part of model initialization. MS Excel was also used for miscellaneous intermediary calculations.
- RT-LAB was used for the adaptation of the developed control system for deployment to the OPAL-RT OP4510.
- A variety of laboratory equipment was used during the development process, testing and experimental verification in different configurations. The laboratory setup is described during work.

Scientific novelties

- Development of an optimized Newton–Raphson-based technique for solving the selective harmonic elimination and selective harmonic mitigation problem for both 2-level and 3-level inverters, improving the accuracy and convergence speed.
- Modification and enhancement of a fundamental current hybrid observer for railway traction drive applications, accompanied by the analysis of its robustness and stability. These modifications extend the work by Prof. J. Holtz [26].
- Introduction and detailed description of a control system that seamlessly transitions between modulation regimes while analysing practical dynamic limits.
- Development of a fully functional control system with low switching frequency specifically designed for railway traction drive applications. The system demonstrates good performance achieved through the implementation of a novel control algorithm.
- Numerical comparison of power module and motor losses in synchronous PWM and selective harmonic elimination PWM.

Hypotheses

- The train traction power converter is hypothesized to reliably operate at a very low switching frequency with a field-oriented control system. This operation is expected to maintain an acceptable level of stator current harmonic distortion while ensuring that the power module losses remain within acceptable limits.
- Selective harmonic elimination PWM is hypothesized to reduce power module and motor losses in comparison to synchronous PWM when subject to a low ratio of switching to fundamental frequencies.

Approbation of research results

Scientific articles and conference papers

1. K. Gulbis, U. Brakanskis, E. Kamolins, M. Gorobecs, A. Potapovs, K. Sejejs, J. Zarembo, and V. **Burenin**, "Analysis of Test Results of the Developed Synchronous Reluctance Motor for Public Transport Application", Latvian Journal of Physics and Technical Sciences, vol. 59, no. 4, 2022, pp. 36–52.
2. A. Suzdalenko, **V Burenin,** J. Zarembo, J. Zakis,. Modelling of Bidirectional Three-Phase Four-Wire Three-Level NPC MLC under Single-Loop Current Sensorless Control. Energies 2023, 16, 4599.
3. **V. Burenin**, J. Zarembo, G. Kobenkins, and O. Krievs, "Implementation of Hybrid PWM with Smooth Transitions between Modulation Modes for Railway Traction Field-Oriented Control System", 2023 IEEE 64th International Scientific Conference on Power and Electrical Engineering of Riga Technical University (RTUCON), Riga, Latvia, 2023, pp. 1–7.
4. **V. Burenin**, J. Zarembo, O. Krievs, and L. Ribickis, "Comparison of Synchronous Reluctance Motor and Induction Motor Efficiency Maps for Traction Application," 2021 IEEE 62nd International Scientific Conference on Power and Electrical Engineering of Riga Technical University (RTUCON), Riga, Latvia, 2021, pp. 1–5.
5. **V. Burenin**, J. Zarembo, A. Žiravecka and L. Ribickis, "Model of Laboratory Test Bench Setup for Testing Electrical Machines," 2020 IEEE 61st International Scientific Conference on Power and Electrical Engineering of Riga Technical University (RTUCON), Riga, Latvia, 2020, pp. 1–5.
6. E. Kamolins, M. Gorobecs, **V. Burenin**, K. Gulbis, A. Potapovs, U. Brakanskis, J. Zarembo, K. Sejejs, "180 kW Synchronous Reluctance Motor for Mass Transit Electrical Traction Application," 2021 23rd European Conference on Power Electronics and Applications (EPE'21 ECCE Europe), Ghent, Belgium, 2021, pp. 1–8.
7. G. Kobenkins, M. Marinbahs, A. Bizans, **V. Burenin,** and O. Sliskis, "Evaluation of the Strength of Traction Geared Motor Units by Permissible Stresses and the Level of Vibration Activity," 2022 International Conference on Electrical, Computer and Energy Technologies (ICECET), Prague, Czech Republic, 2022, pp. 1–6.
8. G. Kobenkins, M. Marinbahs, A. Bizans, N. Rilevs, **V. Burenin,** and O. Sliskis, "Carrying Out of Strength Control of Mutual Loaded Traction Geared Motor Boxes as a Part of

Industrial Tests," 2022 9th International Conference on Electrical and Electronics Engineering (ICEEE), Alanya, Turkey, 2022, pp. 185–189.

9. G. Kobenkins, M. Marinbahs, **V. Burenin**, J. Zarembo, A. Bizans, and O. Sliskis, "Determination of the Level of Own Vibration of Geared Motor Boxes in Industrial Conditions," 2021 IEEE 62nd International Scientific Conference on Power and Electrical Engineering of Riga Technical University (RTUCON), Riga, Latvia, 2021, pp. 1–6.
10. G. Kobenkins, M. Marinbahs, **V. Burenin**, J. Zarembo, and O. Sliskis, "Carrying Out of Strenght Tests of Geared Motor Box as Part of a Frequency-Controlled Traction Electric Drive," 2021 17th Conference on Electrical Machines, Drives and Power Systems (ELMA), Sofia, Bulgaria, 2021, pp. 1–4.

1. Description of the Pre-Programmed PWM

The software of the power traction converter is a complex, interconnected system consisting of control systems, a PWM modulator, communication protocols, various service tools, and more. The PWM technique within the PWM modulator is a critical component, with the two most prominent methods being carrier-based SPWM and SVPWM [24]. However, in high-power applications such as those in railway traction electric drive systems, the switching frequency must be constrained to low values to prevent overheating and premature failure of high-power semiconductors, as the high-power semiconductors have high switching losses at elevated frequencies.

Reducing the switching frequency is a feasible strategy, but the ratio of the switching frequency to the fundamental frequency ($m_f = \frac{f_{sw}}{f_1}$) for SPWM and SVPWM typically does not drop below $m_f = 9$ [27], [28]. Considering that induction motors in traction applications usually have two or three pole pairs with a fundamental frequency reaching 160–180 Hz, this limitation means the switching frequency exceeds 1000 Hz. Yet, usually, the switching frequency for high-power semiconductors is limited to a few hundred hertz up to 1 kHz [6], [16], [17], [18], [19].

A low m_f ratio can degrade the current regulating performance of variable frequency inverters, potentially leading to instability [29]. Moreover, with conventional PWM, the proximity of harmonic orders to the fundamental necessitates bulky filtering devices and can increase losses and torque ripples in the induction motor, especially prominent for harmonics less than the 10th order [22], [23].

These challenges necessitate specialized PWM techniques to limit or eliminate specific harmonics using low switching frequency, thereby extending the life of the traction converter and reducing motor losses. The main method to limit switching frequency and keep a focus on the output harmonic spectrum is pre-programmed PWM (PPWM). Common variations are SHE, SHM, a hybrid of SHE and SHM, and PPWM with optimized switching pulse patterns/sequences [15].

Distinct from conventional modulation strategies like SPWM and SVPWM, which are carrier-based, PPWM instead utilizes gating signals (or switching angles) pre-calculated based on fundamental Fourier transformations and required elimination of predetermined harmonics. These switching angles are calculated by solving a system of nonlinear equations offline and stored in a look-up table for use during operation [24]. This method's main advantage is the generation of higher-quality current waveforms at low m_f values. However, it is primarily suited for low-dynamic power systems, such as trains in this case, due to the limited controller bandwidth [30].

SHE-PWM is the most widely used approach, which eliminates pre-defined harmonics fully from the output waveform by switching at specific points in time. SHM-PWM is very similar in nature to the SHE-PWM. In general, it is a variation of SHE-PWM, where no specific harmonics are eliminated, but overall THD is limited, or specific harmonics have their upper limit different from zero [14], [16], [31]. This method is reported to be used to limit grid codes in accordance with regulations [16], [25], [31], [32]. In other literature, a variation of the selective harmonic mitigation method is called optimized pulse pattern (OPP-PWM), introduced and mainly used by the ABB [33], [34], [35]. The hybrid SHE/SHM combination is used when there is a possibility to switch between these two methods or if there is another goal besides maintaining the current waveform.

For this research, SHE-PWM was selected, which prioritizes the elimination of the lowest harmonic, as harmonics closest to fundamental have the highest effect on current quality and motor losses [22], [23]. The SHE as a technique of modulation gained more attention after the study by Patel and Hoft [36], [37]. However, due to the limited technological capabilities of the power electronics of that time, the described method was difficult to implement and develop.

This chapter summarizes the results of the research of selective harmonic elimination.

1.1. Mathematical basis of the pre-programmed PWM

In scientific and technical literature, the formulations of SHE-PWM are based on decomposing voltage PWM waveforms using Fourier series expansion. The formulation of SHE-PWM typically depends on the characteristics of a given waveform, such as unipolar, bipolar, stepped, multilevel, symmetrical, and asymmetrical waveforms. These features are equally important in analysing and determining the complexity and form of the solution space [15].

During analysis, SHE formulation with the quarter-wave symmetry is used, as it requires the least number of equations and substantially simplifies the calculation process of solving the SHE-PWM problem. The function describing the general Fourier series is:

$$f(\omega t) = a_0 + \sum_{n=1}^{\infty} [a_n \sin(n\omega t) + b_n \cos(n\omega t)] \tag{1.1}$$

However, when following the quarter wave symmetry, only the a_n coefficient for odd harmonics has a non-zero value. In a symmetrical three-phase system, triplen harmonics of phase voltage are co-phasal and equal in magnitude. Thus, for a star-connected motor with an insulated neutral point, the phase voltages will cancel out the line-to-line voltage, and no line current of triplen harmonics will result. These assumptions and physical properties greatly simplify the solutions process, as in this case, the a_n coefficient is a relative value of harmonics amplitudes of output phase voltage of $n = 5, 7, 11, 13$ ... order.

Upon determining whether the obtained voltage waveform fulfils the conditions of a quarter-wave symmetry and based on the Fourier series it is possible to create a system of N equations (1.2) [25].

$$\begin{cases} \dfrac{4}{n_1\pi}[1 - 2\cos(n_1\alpha_1) + 2\cos(n_1\alpha_2) - \cdots \pm 2\cos(n_1\alpha_N)] = M_1 \\ \dfrac{4}{n_2\pi}[1 - 2\cos(n_2\alpha_1) + 2\cos(n_2\alpha_2) - \cdots \pm 2\cos(n_2\alpha_N)] = 0 \\ \vdots \\ \dfrac{4}{n_N\pi}[1 - 2\cos(n_N\alpha_1) + 2\cos(n_N\alpha_2) - \cdots \pm 2\cos(n_N\alpha_N)] = 0 \end{cases} \tag{1.2}$$

Each of the above-mentioned equations is used to fix an amplitude for a selected voltage harmonic. This set of equations for N switching angles allows for eliminating $N - 1$ voltage harmonics and determining the M_1 value of a basic component, defined by the relation

$$M_1 = \frac{2 \cdot V_{ph}}{U_{dc}}, \tag{1.3}$$

where V_{ph} is the eligible amplitude of an output voltage basic component.

In Formula (1.2), Equations 2 – N have their right sides compared to zero, which is equivalent to the application of the SHE method. If the right sides of a set of equations (1.2) are replaced by the vector of values of the selected harmonics, there is an opportunity to set values of the selected harmonics (SHM technique). Using the method of SHM gives a wide range of shaping opportunities for an inverter's output voltage harmonics and, consequently, the DC-link current harmonics spectrum [25].

1.2. Development of solving algorithm

The numerical method for the solution of a set of nonlinear transcendental equations is based on the study of Patel and Hoft, 1973, [36] with several modifications, and uses a Newton–Raphson method. The correct solution must satisfy the condition stated below. To solve the system, it must satisfy the condition as it ensures physical feasibility and non-singularity of the solution.

$$0 < \alpha_1 < \alpha_2 < \cdots < \alpha_N < 90° \tag{1.4}$$

When solving a set of nonlinear equations numerically, the primary concern is the convergence of the method used. Unlike solving a single nonlinear equation, where many methods exist for obtaining a priori information on the root's location, there is no single approach for determining an initial guess in a system of nonlinear equations. Without a way to obtain a priori information, convergence becomes an issue, as the solving process often leads to divergence. It is usually a trial-and-error process, and no general method exists that can guarantee convergence to a solution [36].

The main implementation details of the algorithm are as follows:

1. **Newton–Raphson Method**: The Newton-Raphson method is employed to solve the system of nonlinear equations derived from the harmonic elimination criteria. The method iteratively refines guesses for the switching angles until a solution is found that satisfies the equations within a specified tolerance.
2. **Solution “unwinding” Approach**: The improved Newton–Raphson algorithm introduces a novel approach to verify and accept solutions, utilizing the inherent properties of trigonometric functions within the system of nonlinear equations. This method ensures the correctness of identified solutions, enhancing both convergence rate and calculation speed.
3. **Parallel Processing**: The script leverages MATLAB's *PARFOR* loop for parallel processing, enabling simultaneous computation of solutions for different modulation indices or sets of equations, significantly speeding up the computation.
4. **Flexibility and Configurability**: The program is designed with flexibility in mind, allowing the user to select 2- or 3-level inverter architecture, easily adjust the harmonics to eliminate, the range and step size of modulation indices to investigate, and calculate the computational accuracy and performance parameters.

To enhance the likelihood of identifying all possible solutions to the system of nonlinear equations, the program is set to run multiple times. This iterative strategy helps to thoroughly explore the solution space. Upon program completion, it saves all unique discovered solutions into an Excel file. The purpose of this step is to facilitate a subsequent manual review process, during which these unique solution sets are separated and analysed. This approach is designed to maximize the comprehensiveness of our solution discovery process, providing a foundation for further analysis and application of the results.

1.3. Application of solving algorithm

The developed algorithm was tested for its performance, convergence, and success rate in finding solutions. This subchapter summarizes the main outcomes.

Found solutions have been systematically recorded in a look-up table for subsequent application in modelling and laboratory testing. The number of solutions found for the 2-level inverter, which correlates with the number of angles (or $N-1$ harmonics to be eliminated), is presented in Table 1.1.

Table 1.1

Number of SHE Solutions for a 2-Level Inverter

SHE angles	Solutions
3	2
5	2
7	4
9	4
11	8
13	8

Initial observations from the presented SHE solutions indicate that all identified solutions for the 2-level inverter are continuous across the specified range of modulation indices, up to and including SHE 13. The harmonic analysis confirms the complete elimination of the targeted harmonics. Typically, the immediate non-triplen harmonic following the highest eliminated harmonic shows an increase, which aligns with expectations.

Moreover, as per design, the generated waveform exhibits quarter-wave symmetry, automatically nullifying all even harmonics. Triplen harmonics are present in a phase voltage waveform. However, in a 3-phase electric machine, line voltage is measured, which cancels all triplen harmonics due to inherent system properties.

All found solutions are viable for achieving low-frequency operation without unwanted harmonics. Notably, some identified solutions resemble the 60° discontinuous PWM pattern (also referred to as DPWM1-3 in some studies) [38], [39], [40]. These solutions avoid switching events for at least 60 consecutive degrees, potentially offering a further reduction in switching losses.

1.4. Performance of solving algorithm

Various solutions obtained through different iterations of the algorithm were explored, including the use of MATLAB's *fsolve* function from the Optimization Toolbox. This section summarizes the performance analysis of the refined algorithm and its comparison to algorithm iterations and the *fsolve* algorithm.

The evaluations were conducted using three algorithmic variations and with the *fsolve* algorithm, each set with identical parameters:

- **Unoptimized Version** utilizing a *PARFOR* loop;
- **Optimized Version** using a standard *FOR* loop;
- **Optimized Version** with a *PARFOR* loop;
- ***fsolve*** algorithm.

The *PARFOR* loop specifically facilitated parallel execution of runs across the available processor cores, which in this case amounted to 4. This parallelization is particularly advantageous when managing a higher number of harmonics as the solving difficulty increases. During the development of the current implementation of the Newton–Raphson algorithm for this specific application, the in-built MATLAB *fsolve* function was employed as a benchmark to gauge comparative performance. The settings for *fsolve* were chosen to mirror those of the primary algorithm.

The initial trials to solve the SHE/SHM equations utilized MATLAB's Optimization Toolbox *fsolve* function. *Fsolve* effectively replaced the Newton–Raphson algorithm as the core of the main program.

Based on the performance results, the *fsolve* method surpasses the computation speed of the unoptimized algorithm but lags behind the optimized version. The stark differences in performance are due to the reliance on the unoptimized and *fsolve* algorithms on condition (1.4) for validation checks, contrasting with the internal optimizations based on trigonometric identities used in the developed algorithm. Such internal checks are not feasible with *fsolve*, highlighting the flexibility and simplicity of the Newton–Raphson method employed in the study.

The unoptimized algorithm ran solely within a *PARFOR* loop to speed up the computation time. For instance, solving SHE 9 scenarios takes over an hour if executed in a *FOR* loop. This duration could extend beyond four hours when a higher number of harmonics are to be eliminated. SHE 13 was also run for a complete picture. However, the unoptimized algorithm has a very low convergence rate, which brings it to the limit of allowed iterations while being unable to find most of the solutions.

The principal determinant of algorithm speed is the total number of function evaluations: optimization within this aspect drastically reduces computation time. For example, for SHE 7, the optimized version reduces the number of iterations by 90.8 % compared to *fsolve* and 98.5 % compared to the unoptimized version.

To fully understand the development of the SHE/SHM algorithm, we introduce two additional performance metrics: convergence rate and success rate.

Convergence rate: A ratio between the number of times a solution is found during a run and the number of times when $iter_{MAX}$ limit is reached (no solution found). Specifically, if no solution is identified after a predetermined number of guesses, the system is flagged as "unable to converge".

Success rate: Unlike the convergence rate, the success rate measures the proportion of the total number of solutions found against the total number of expected solutions.

Analysis of the data reveals that while *fsolve* generally exhibits higher convergence and success rates across all SHE scenarios, it is significantly slower – taking 10 to 15 times longer – and requires more function evaluations than the optimized algorithm.

It should be noted that the time when transitioning from SHE 9 to SHE 11, and even to SHE 13 in an unoptimized algorithm, does not increase exponentially. That is because the algorithm is very close to pre-defined limits of iterations, and the convergence rate is very low, at only 5.4 % and 0.5 %, respectively. An unoptimized algorithm requires widening limits to find all the solutions, as the convergence rate is very low.

1.5. Conclusions

This chapter has detailed enhancements to the Newton–Raphson algorithm for solving SHE and SHM problems in both 2-level and 3-level inverters. The optimized algorithm proves superior to the generic *fsolve* function in terms of both the computation time per iteration and the total number of iterations required to reach a solution. Further improvements, such as an adaptive number of runs, could enhance the algorithm's speed.

The optimization process within the algorithm primarily occurs during the solution verification phase, even though the initial guesses are randomly generated within the constraints of condition (1.4). To generate initial guesses, there is no straightforward method to acquire a priori information that would allow for a more targeted initial guess range [15].

It is important to emphasize that the speed of calculation provided by the optimized algorithm is particularly advantageous in SHM, where minimizing THD or complying with grid codes takes precedence over mere harmonic elimination in SHE. This methodology necessitates multiple recalculations of switching angles at different harmonic level references to optimize a specific cost function. When addressing higher values of switching angles, the optimized algorithm speeds up work in the calculation stage or allows for improved step fidelity.

2. Control System Development

The design of the control system, which incorporates a hybrid PWM algorithm, is a core aspect of this research. This chapter summarized the design process of the traction electric drive and control system. The design process includes several crucial steps:

1) analysing the application, parameters, and requirements for both the vehicle and the motor;
2) developing the hybrid PWM modulator;
3) designing and implementing a control system tailored to the specific needs of the application.

2.1. Electric multiple unit

Railway vehicles come in a multitude of different varieties, the most common of which are trams, metros, trains, and locomotives. Each type has its own set of specifications, including but not limited to supply voltages, motor output power requirements, number of cars, weight, and top speeds.

For this research, the analysis is narrowed to trains, specifically electric multiple units (EMUs), as they represent a common application for medium-voltage high-power converters. Common parameters for EMUs include [4]:

- supply voltages: 750 V DC, 1500 V DC, 3000 V DC, 15 kV AC (16.7 Hz), 25 kV AC (50 Hz);
- electric motors power: 200–600 kW;
- traction converter power: 200–1400 kW;
- number of cars: 2–12;
- top speed: 120–350 km/h.

The market analysis is done to determine the average parameters of the EMUs in service. The analysis focuses predominantly on the use of EMUs in intercity and regional rail networks in Eastern Europe with a supply voltage of 3000 VDC. The 3 kV DC power supply voltage is one of the dominant power networks, accounting for 44 % of the market (combined with 1.5 kV DC) [41] and is utilized in countries such as Latvia, Estonia, Poland, Netherlands, Ukraine, Russia, Italy, and parts of Spain and France [42].

Market research was conducted on the EMUs used in the 3 kV DC grid from several prominent producers: Newag (Poland), Pesa (Poland), Škoda (Czech Republic), CAF (Spain), and Stadler (Switzerland). The purpose of this comparative analysis is to outline the main variations of EMUs used in the region by comparing the continuous power of the train to its mass, and the gross weight of the train per single motor. These parameters are crucial for the selection and/or design of an appropriate traction motor. The power-to-weight ratio and mass per motor will be averaged and used for selecting the traction motor.

Averaging many parameters can be challenging due to their dependence on various EMU configurations, such as the number of motors per set, the number of cars per set, and motor power. Nevertheless, mass per motor and continuous power-to-weight ratios are commonly utilized to assess the comparative performance of vehicles in general. Setting the desired requirements involves considering the customer's needs, the geography of operation, and other complex factors. However, for the purposes of this research, average parameters suffice for the design of the control system.

- Average mass per motor: **38.9 tons/motor**.
- Average power-to-weight: **11.2 W/kg**.
- Common average acceleration in the constant torque regime of the induction motor: **1 m/s^2**.

These parameters are used to estimate the dynamic parameters of a train equipped with the selected traction induction motor.

2.2. Traction motor

The selection and/or design of a traction motor is a complex process tailored for specific vehicles. The design process for the traction motor involves several key considerations to achieve a cost-effective balance among various factors. These considerations include:

- understanding the vehicle's geometrical and mounting constraints;
- addressing the dynamic requirements of the vehicle,
- Managing adhesion constraints and environmental usage conditions;
- considering wheel diameter and maximum speed;
- selecting gearbox ratio, type, and producer;
- determining the cooling approach;
- evaluating financial implications, among others.

Typically, traction motors are custom-made for EMU producers in collaboration with companies specializing in traction motor production. Detailed parameters of these motors are often confidential. However, the research and development project at JSC "Rīgas elektromašīnbūves rūpnīca" has provided access to detailed parameters and testing results of the traction induction motor prototype for EMU application. These parameters and the maximum traction characteristics are used for simulation.

The developed traction motor is a squirrel cage 3-phase, 4-pole, star-connected induction motor. The main parameters of the motor, operating with S1 (continuous) duty, are presented in Table 2.1.

Table 2.1

S1 Working Point Parameters

Parameter name	Units	Value
Output power (on shaft)	kW	360
Stator voltage LL	V	2340
Stator current	A	107.4
Power factor	-	0.886
Frequency	Hz	79.5
Slip	%	1.06
Rotational speed	RPM	2359.8
Mechanical torque	Nm	1456.8
Maximum torque	Nm	3925.6
Efficiency	%	93.1
Current, slip = 0	A	35

The maximum speed of the motor is 4774 RPM, with an insulation class of 220 °C.

To obtain equivalent circuit parameters, the motor was tested according to IEC 60034-28:2012 [43]. These parameters are detailed in Table 2.2.

Table 2.2

Equivalent Circuit Parameters

Parameter name	Units	Value
Stator resistance at 20 °C	mΩ	166.3
Rotor resistance at 20 °C	mΩ	101.5
Stator leakage inductance	mH	2.23
Rotor leakage inductance	mH	2.80
Magnetizing inductance	mH	77.05

Table 2.3 shows the mechanical parameters of the induction motor. For the design of the speed control of the control system, inertia is the most important part. These parameters are obtained based on the deceleration test [44] and based on the known geometry of the electrical machine.

Table 2.3

Mechanical Parameters

Parameter name	Units	Value
Inertia of the rotor	kgm^2	8
Viscous friction coefficient	Nms/rd	0.02

The next crucial part is the traction limits imposed on the motor and control system. The reference traction characteristic of the electrical traction motor represents the maximum effort of the motor during normal acceleration. Creating such a limiting traction characteristic involves understanding the motor's thermal limits, converter current limits, the used gearbox, and the vehicle's dynamic requirements. The traction effort limit is a part of the electrical-mechanical characteristics of the motor, depicting output power, torque, line voltage, and stator current at maximum effort, as shown in Fig. 2.1.

Traction characteristic has the following regions:

1) 0–350 RPM: torque is limited to the value achieved when stator current is limited to 250 A RMS;
2) 350–1720 RPM: constant torque region limited by $T_{out} = 3000$ Nm;
3) 1720–3310 RPM: constant power region limited by $P_{out} = 540$ kW;
4) 3310–4780 RPM (max speed): $T_{elm}\omega_m \cong constant$ or $T_{em} \propto \frac{1}{\omega_s^2}$ region.

Additionally, at the value of torque during traction characteristic (at 2427 Nm) and at a speed of 2130 RPM, stator line voltage reaches a nominal value of 2340 V RMS. Below 2130 RPM, it keeps a nominal flux of 2.9 Vs, and above 2130 RPM, the motor goes into a field-weakening regime. With an implemented feedback-based field weakening controller, this speed point varies slightly depending on the load.

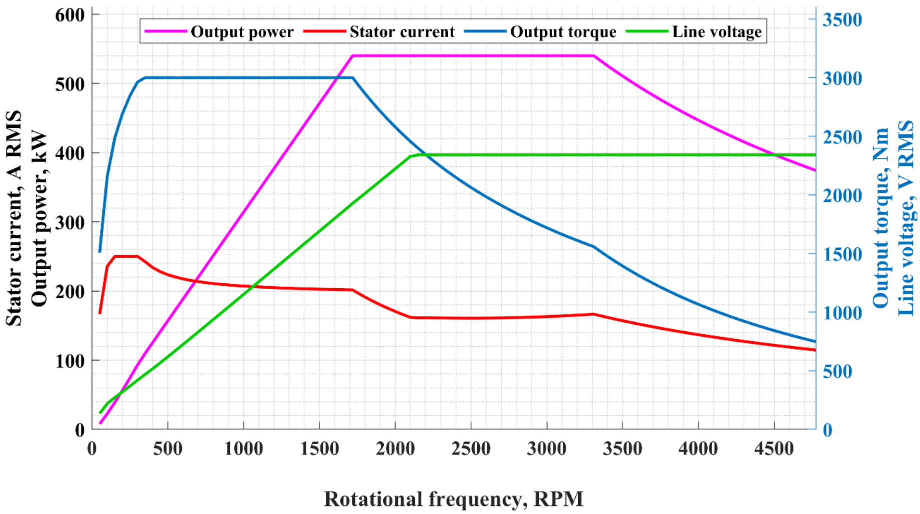

Fig. 2.1. Reference traction characteristic of the induction motor.

The characteristic was developed for the actual motor prototype. The output power in the constant region is 540 kW, which is 1.5 times higher than in S1 duty. This is because the motor does not operate at this power most of the time but only during maximum effort acceleration and deceleration.

The last step in the process is the determination of the dynamics of the vehicle based on traction characteristics and vehicle parameters. However, all these parts are interconnected, as the creation of the limiting traction characteristic is always tailored to the vehicle.

Railway vehicles are generally treated as semi-rigid bodies, described by their linear and angular position along three coordinated dimensions. For this research, only the longitudinal motion is considered. The mathematical model is based on the approach by A. Sciaretta and A. Vahidi (2020) [45], with detailed implementation shown in prior research by the author [46]. Key vehicle parameters include:

- Average gross mass (including passengers) per motor: 38.9 tons/motor.
- 2 motors per car.
- Train resistance: $w_o = 0.6 + 0.027 \cdot v + 0.00005 \cdot v^2 [\mathrm{N/kN}]$ [47].
- Inertial mass ratio: $\gamma = 1.08$ [41], [47], [48]. It is different for different train types and configurations. 1.08 is a commonly used value for intercity and regional EMUs.
- Wheel diameter (commonly used): 0.85 m – new, 0.78 m – worn out.
- Gearbox ratio: 5.89, chosen to ensure a maximum operating speed of 120 km/h even with worn-out wheels.

Based on these parameters, the train is calculated to have:

– power-to-weight ratio: 9.3 W/kg;
– maximum acceleration: 0.95 m/s^2;
– average acceleration from 0 to 50 km/h: 0.89 m/s^2, and time to reach 50 km/h is 15.7 seconds;
– acceleration from 0 to 120 km/h with a new wheel: 59.4 seconds.
– maximum speed with new wheel – 130 km/h, with worn out wheel – 120 km/h.

This calculation uses average parameters, but the actual induction traction motor application will require adjustments to the motor's outer casing for mounting and changes to crucial parameters such as train car weight, gearbox ratio, and dynamic requirements.

This calculation serves solely as a reference for the design and development of the control system methodology. Based on this methodology, any other combination of train, motor, and power converter parameters could be used to achieve the required result.

2.3. Power converter

Besides the traction motor, the power converter is another important component of the traction drive. As previously discussed, this research implements a hybrid PWM approach aiming to limit

IGBT and diode losses within junction temperature limits while reducing harmonic currents compared to conventional modulation methods.

An important part of the research involves the precise calculation of IGBT module losses. This accuracy is essential to assess the impact of PWM types not only on the stator's current quality but also on the converter's losses.

Only losses are calculated, not the junction temperature, as temperature calculation requires an understanding of the utilized heatsink and cooling solution. These factors are highly application-dependent and are typically designed based on the hardware configuration of the actual implementation, often modelled using FEM analysis with specialized software. However, losses are sufficient for comparative analysis of different modulation strategies.

Power module losses

During frequency inverter operation IGBT operates as a switch with anti-parallel freewheeling diode, taking on various static and dynamic states in cycles. In any of these states, one power dissipation or energy dissipation component is generated, heating the semiconductor and adding to the total power losses of the switch [49]. Fig. 2.2 shows the individual power losses of semiconductor switches.

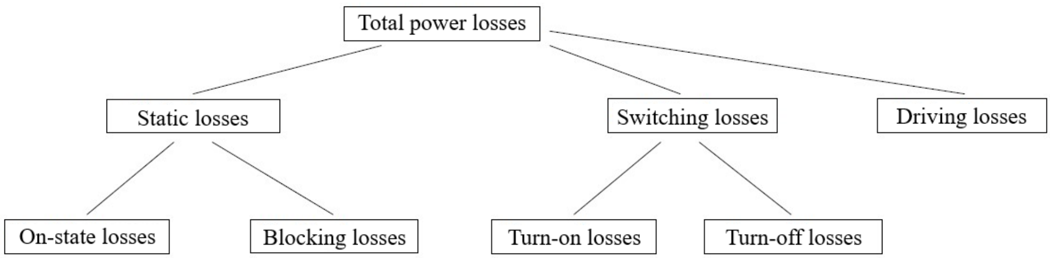

Fig. 2.2. Individual power losses of semiconductor switches [49].

The calculation methodology is based on Semikron's application manual [49].

IGBT power module

ABB is one of the leading producers of both power converters for railway applications and IGBT power modules used in power converters. Therefore, for specific calculation of converter losses, one of the power modules with a freely available datasheet is selected, matching the power demand and breakdown voltage requirements.

ABB HiPak 5SNA 0600G650100 IGBT power module is selected and used [50] for losses calculation, with parameters for the IGBT turn-on, turn-off, and conduction losses, and diode turn-on (recovery) and conduction losses in XML format available from the manufacturer's website [51], [52]. This power module has a 6.5 kV rated blocking voltage and is designed for a collector current of 600 A.

From the producer’s data of IGBT and diode, the power module’s switching and on-state/forward characteristic models are created.

Losses calculation approach

Losses calculation is done instantaneously at each discrete calculation step. Losses are calculated separately for IGBT and diode. For the analysis and comparison of PWM approaches, losses are averaged over each fundamental period over several fundamental periods.

The calculation function takes approximation model coefficients, DC-link voltage, stator phase current, and corresponding IGBT pulse. An in-depth description and the model coefficients are laid out in the full text of the Thesis.

2.4. PWM modulator

The next major component in the design of the control system is the PWM modulator. As previously described, hybrid PWM combines several distinct PWM regimes: asynchronous, synchronous, and SHE PWM. This subchapter briefly summarizes key details of the PWM modulator implementation.

The modulator is designed to allow for maximum flexibility and hardware deployment. The modulator consists of asynchronous/synchronous SVPWM module and SHE PWM module with mode selection and hysteresis. Each module is executed iteratively at each time step to create a pulse train suitable for the inverter. The PWM module allows for mode selection and smooth transitions between them.

PWM transitions only when the reference voltage sinewave crosses zero in the positive direction (phase of 0°) to ensure smooth phase following.

Additionally, a small hysteresis band (0.5–1 Hz) is added to avoid jitter when the system is stable near the transition point. Mode transition points and limiting switching frequency are one of the system inputs and, in actual application, are chosen based on converter power module losses in order to stay within junction temperature limits.

Overall system inputs include the reference three-phase sine wave, synchronous frequency, and mode transition points. The system outputs pulses for the converter and the current PWM mode.

2.5. Control system

The control system is the heart of a traction electric drive. The primary objective for traction applications is speed control, with field control in the field-weakening regime. During this study, based on previous research, the field-oriented control (FOC) system is used. FOC systems enable precise real-time control of the electric machine's state.

The FOC system requires the fundamental component of the stator current or stator flux as a feedback signal. Such signal is inherently obtained as part of the modulation algorithm when carrier-based modulation is used [53]. However, in contrast to carrier-based modulation, PPWM strategies do not offer this feature since the measured and sampled current contains significant harmonic content [54].

Various methods have been developed to estimate the fundamental current component, such as filtering, model-predictive control (MPC), and different observer variations. Filtering is not appropriate for applications requiring high dynamic performance. MPC combined with PPWM is an effective but computationally intensive method, enabling a very fast dynamic response without needing a complex observer [54]. In this case, a simple type of hybrid observer is implemented, which estimates the fundamental current, rotor flux, and torque. The hybrid observer design is based on the study of J. Holtz and N. Oikonomou (2008) [26], with several key improvements and custom code implementations.

This chapter summarizes three parts of the control system development:

- field-oriented control system and overall traction drive schematic;
- back-emf and cross-coupling decoupling;
- hybrid observer
- control design (tuning of PI controllers).

Field-oriented control

FOC decouples the effects of the torque and magnetizing flux in the stator current. These decoupled currents are used to independently control torque and maintain magnetization at the required level, making control quite similar to that of a DC machine [55], [56].

FOC operates on the technical principle of transforming a three-phase, time- and speed-dependent system into a rotating (d, q) coordinate system that is time-invariant. This transformation is achieved using Park and Clarke transformations. By dealing with instantaneous readings in this transformed frame, FOC ensures precise and accurate control. One of the main advantages of FOC is its ability to reach torque and flux references independently. Torque can be directly controlled by keeping the rotor flux constant and manipulating only the torque component of the stator current vector. This relationship is expressed in Equation (2.5) [55] if flux is kept constant, torque and the quadrature component of stator current are linearly dependent.

$$T \propto \psi_r i_{sq}, \tag{2.5}$$

where T is torque, ψ_r is rotor flux, and i_{sq} is the quadrature component of the stator current.

The core of the implemented FOC control system is classical. It takes inputs such as reference speed, measured feedback speed, and measured stator current and outputs three-phase voltage per unit along with the modulation index for the PWM modulator. The system includes five PI regulators: speed, flux, field-weakening, and one for each component of the stator current.

FOC requires precise transformation from the stationary reference frame to the rotor-oriented rotating reference frame. This transformation necessitates an accurate current frequency, which is non-trivial for induction motors due to slip, which is not directly measurable. Typically, a rotor model is used for rotor angle estimation. In this implementation, the rotor angle estimation is incorporated into the estimation of the fundamental current by the hybrid observer.

Back-emf and cross-coupling decoupling

Back-emf and cross-coupling decoupling are also considered in the FOC system based on the work of Abad(2017) [4]. They can act as disturbances for the current controllers or be compensated for, thus making the relationship between the d and q components of the stator current and voltage correspond to an RL load (i.e., a first-order system) [4]. With proper current regulator designs, accurate, high-bandwidth control of the current is possible. Moreover, the current regulator design is greatly simplified when considering a first-order system.

Fundamental current hybrid observer

The FOC system for fast control requires a fundamental component of the stator current as a feedback signal. Such signal is inherently obtained as part of the modulation algorithm when carrier-based space-vector PWM is used. Pre-programmed PWM, such as the considered SHE/SHM PWM, does not provide a comparable feature. This means that by regular sampling, it is not possible to acquire a fundamental waveform; it will be highly distorted.

To operate FOC, a hybrid observer has been implemented for the identification of the fundamental current. The fundamental current hybrid observer used has been introduced by Professor J. Holtz and N. Oikonomou in 2008 [26]. Several modifications were made, while making custom implementation.

Observer hybrid structure is the combination of the stator model of the induction motor in stationary coordinates and the rotor model in rotor field coordinates. Fig. 2.3 represents a diagram summarizing the structure of the hybrid observer in the form of a flow diagram for visualization of interconnections. The hybrid observer is implemented in Simulink in the form of a function and tested. The function is made in a way to easily adapt it to microcontroller implementation.

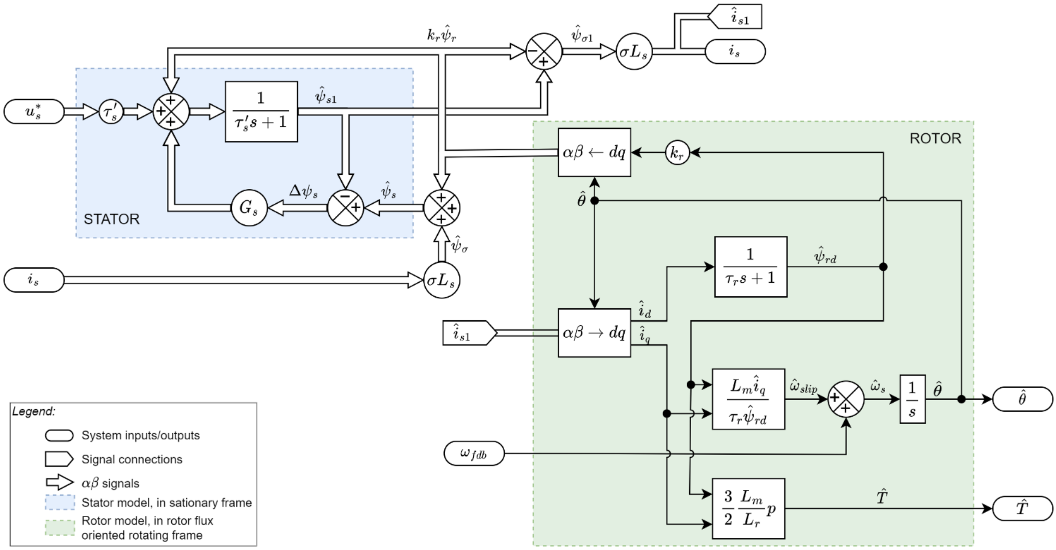

Fig. 2.3. Flow diagram of the hybrid observer.

In summary, the hybrid observer function has:

Inputs: measured stator current, command voltage vector and measured mechanical speed.

Outputs: d- and q-axis estimated stator currents, rotor flux, electromagnetic torque, synchronous speed and rotor angle.

Controller design

A proper control system design requires precise tuning of the controllers used to generate voltage commands for the frequency inverter. PI regulators implemented in a synchronous reference frame are widely accepted as the standard solution for current regulation in vector-controlled AC drives [4]. Proper tuning of these PI controllers, based on a thorough understanding of the machine model, is crucial for the stable operation of the traction electric drive across all operating regimes.

The implemented FOC system has two parallel feedback control loops; each loop has two cascades.

- Loop 1: A d-axis current controller and a flux controller, with a field-weakening controller acting above the nominal point.
- Loop 2: A q-axis current controller and a speed controller.

In a control system with cascaded feedback loops, the analysis typically begins with inner loops, which are progressively reduced to simplify the system to a single closed-loop transfer function [57]. This reduction is feasible because the time constants of the inner (current) and outer loops (speed and flux) differ significantly for high-power electric machines due to the physical nature of the mechanical systems, thereby simplifying the tuning process. Parallel loops of flux and speed are also considered separately because decoupling is performed to separate the effects of each other to a minimum and simplify the control system design.

The design of a field-oriented control system involves three general steps:

- tuning of d- and q-axis stator current controllers;
- tuning of speed controller (just motor, and with a vehicle);
- tuning of flux controller.

The d- and q-axis controllers use the same set of gains because the induction motor exhibits similar dynamics for both d- and q-axis currents. The controller design involves selecting the controller type (in this case, all regulators are PI) and defining the optimal settings. The parameters are chosen according to established criteria. The optimal modulus criterion (OMC) and optimal symmetry criterion (OSC) are commonly used in power electronics and drive control practices. The OMC is used for tuning the inner loop, while the OSC is usually applied to the outer loop [58], [59]. However, in this case, the response of the outer loop is selected directly based on the desired bandwidth and damping of the system [4].

The control design approach and methodology are based on references [4], [57], [58], [59] and rely on the transfer function of the constituent components of the system.

Control design and calculations are made in MATLAB with the Control System Toolbox. The transfer function is created using '*tf*', step response is obtained using the '*step'* function, custom input system response is done with *'lsim'* function, and information about overshoot and settling time with '*stepinfo*', closed-loop transfer function for step response calculation is constructed using the '*feedback*' function.

The tuning of the controller is omitted in the summary as it follows common approaches to the design, which are described in the full version of the Thesis. Table 2.4 summarizes the results of the design process in tabular form for an understanding of the utilized controller parameters.

Table 2.4

Summary of the Controller Coefficients

<table>
<tr><th>Controller</th><th>T_i</th><th>$k_i = \frac{k_p}{T_i}$</th><th>k_p</th><th>Rise time</th><th>Settling time</th><th>Overshoot</th></tr>
<tr><td>d-/q- current</td><td>13.3 ms</td><td>121.8</td><td>1.62</td><td>4.3 ms</td><td>17.4 ms</td><td>4.9 %</td></tr>
<tr><td>Speed (motor)</td><td rowspan="2">141.4 ms</td><td>800</td><td>113.1</td><td rowspan="2">78.5 ms</td><td rowspan="2">476.1 ms</td><td rowspan="2">22.3 %</td></tr>
<tr><td>Speed (EMU)</td><td>22470</td><td>3177</td></tr>
<tr><td>Flux</td><td>134.4 ms</td><td>580</td><td>78</td><td>105.9 ms</td><td>540.8 ms</td><td>16.3 %</td></tr>
<tr><td>Field-weakening</td><td>134.4 ms</td><td>20.1</td><td>2.7</td><td></td><td></td><td></td></tr>
</table>

3. Simulation of Traction Drive System with Hybrid PWM

This chapter summarizes the simulation of the traction drive model with a designed control system. It aims to assess the performance and capabilities in both static and transient regimes of operation and to verify the stability of the control system before proceeding to experimental verification.

All tests have identical hybrid PWM transition types and points of transition unless otherwise specified. The utilized hybrid PWM transition scheme is shown in Fig. 3.1.

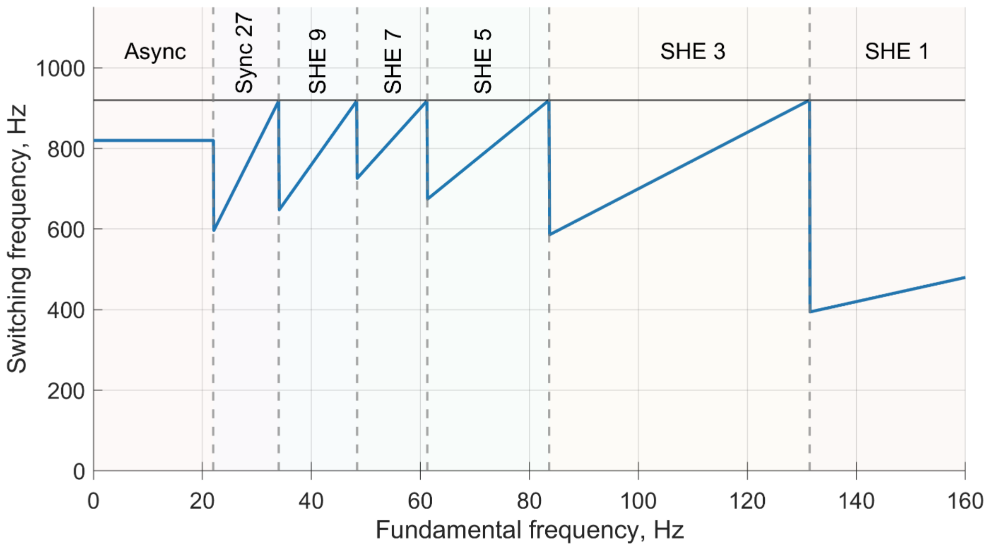

Fig. 3.1. Hybrid PWM transitions scheme (used in simulation).

3.1. Analysis of stator current harmonic content and converter losses

This subchapter focuses on harmonic analysis of the induction motor stator current and power converter losses in static operation. Several tests were carried out to depict the total harmonic distortion (THD), weighted total harmonic distortion (WHTD) and converter losses while outlining the differences between modulation modes.

The analysis is done using the FFT functionality of MATLAB; after that, for visualisation and comparison purposes, harmonic grouping was done based on the IEC 61000-4-7:2002 standard [60]. Each signal is analysed with integer harmonic order grouping, from 1st to 50th harmonic.

THD and WTHD calculations are done according to the study of D. Holmes and T. Lipo (2003) [28]. THD is the most common measure of waveform distortion, while WTHD is more useful in comparing different switching algorithms, as it takes into consideration the value of each harmonic as a weight, as the further the harmonic is from the fundamental, the lesser effect it has on losses in the induction motor. However, it is useful only in comparison to other PWM regimes. Additionally, stator current fundamental harmonic amplitude (I_1), and harmonic current content component up to the 50th harmonic ($I_{2...50}$) are shown in each test. Harmonics are considered and analysed up to the 50th order, as above, that effect on losses and WTHD is almost negligible.

Overview of modulation performance in static regime

The first test is a representation of harmonics and losses in each modulation regime in static conditions. This test serves as a baseline test for the operation of the PWM module. It aims to provide harmonic content and specific harmonics in each regime and constituent power module losses while setting the stage for further tests and comparison.

Table 3.1 provides an overview of used reference points. TrChar is the traction characteristic reference from Fig. 2.1. Loading conditions: no-load marked as (A), 50 % of traction characteristic reference marked as (B), and full traction characteristic reference marked as (C). The left column shows the reference torque, and the right column shows the switching frequency. PWM modes are marked (1) through (7) correspondingly for more concise naming in the following tables.

Table 3.1

Overview of Reference Points

PWM mode	**Reference speed, RPM**	**Reference torque, Nm | Switching frequency, Hz**					
		No-load (A)		0.5 TrChar (B)		TrChar (C)	
Asynchronous (1)	600	0	820	1500	820	3000	820
Synchronous 27 (2)	900	0	810	1500	831	3000	852
SHE 9 (3)	1200	0	760	1500	775	3000	789
SHE 7 (4)	1650	0	825	1500	837	3000	848
SHE 5 (5)	2100	0	770	1228	777	2456	784
SHE 3 (6)	3000	0	700	859	706	1718	714
SHE 1 (7)	4200	0	420	484	423	968	427

Table 3.2 outlines the stator current performance indicator of the stator current in each modulation regime and at each loading condition, while Fig. 3.2 provides FFT with integer grouping of up to the 50th harmonic.

From the current performance indicators, it could be seen that at fully loaded conditions THD and WTHD are not that high, with relatively low values of harmonic content. However, harmonic content stays relatively consistent despite the load. Meaning that at no load, harmonic values are comparable to the fundamental and could be even higher with SHE 1.

Table 3.2

Summary of the Stator Current Indicators

Mode /Load	THD, %			WTHD, %			I_1			$I_{2...50}$		
	(A)	(B)	(C)	(A)	(B)	(C)	(A)	(B)	(C)	(A)	(B)	(C)
(1)	8.37	8.13	2.42	1.45	3.16	0.65	54.2	144.5	275.1	4.5	11.7	6.7
(2)	14.54	8.35	3.99	2.39	2.59	0.87	54.0	144.8	274.7	7.9	12.1	11.0
(3)	49.82	19.18	9.69	2.23	2.36	0.75	53.9	144.9	274.8	26.8	27.8	26.6
(4)	42.72	16.07	7.65	1.99	2.32	0.71	53.7	145.0	274.5	23.0	23.3	21.0
(5)	47.73	20.23	10.76	2.79	1.76	1.81	53.8	122.9	227.0	25.7	24.9	24.4
(6)	53.43	16.69	7.82	4.35	1.82	0.78	34.0	109.4	229.3	18.2	18.3	17.9
(7)	201.81	53.15	24.67	35.37	9.34	4.50	22.7	85.8	185.7	45.8	45.6	45.8

Fig. 3.2 expands the results in Table 3.2 by providing the location of each harmonic in each respective regime, and each tile shows harmonics at each load.

It can be seen that modulation regimes are working as expected. Asynchronous PWM has harmonics to the side of 820 Hz. However, they drift in harmonic order depending on the slip. But synchronous PWM has 25th and 29th harmonics to the sides of the 27th and they are independent of slip, as the frequency is synchronized with the synchronous speed.

SHE reliably eliminates all the lower-order harmonics while boosting the following non-eliminated ones. From these results it could be seen that each SHE regime operates as expected.

Fig. 3.3 outlines constituent power module losses in each regime and loading condition. As expected, in the high-power IGBT/Diode module, the majority of the losses are produced by the switching losses, with the share of IGBT and diode conduction losses being 15–20 % at the heaviest load. It once again shows that the focus here is the limits of switching losses by means of limiting switching frequency in these devices.

Following that, based on the results several preliminary conclusions could be drawn. While THD with SHE PWM is substantially higher than the one with synchronous PWM, WTHD is almost the same because the harmonic order is shifted further from the fundamental harmonic and is less critical. It has a lesser effect on the motor losses and could be more easily filtered. At the same time, when transitioning from sync. 27 to SHE 9, switching frequency is lowered by 6.2–7.4 %, and total power losses are lowered by 4–8 % based on loading conditions.

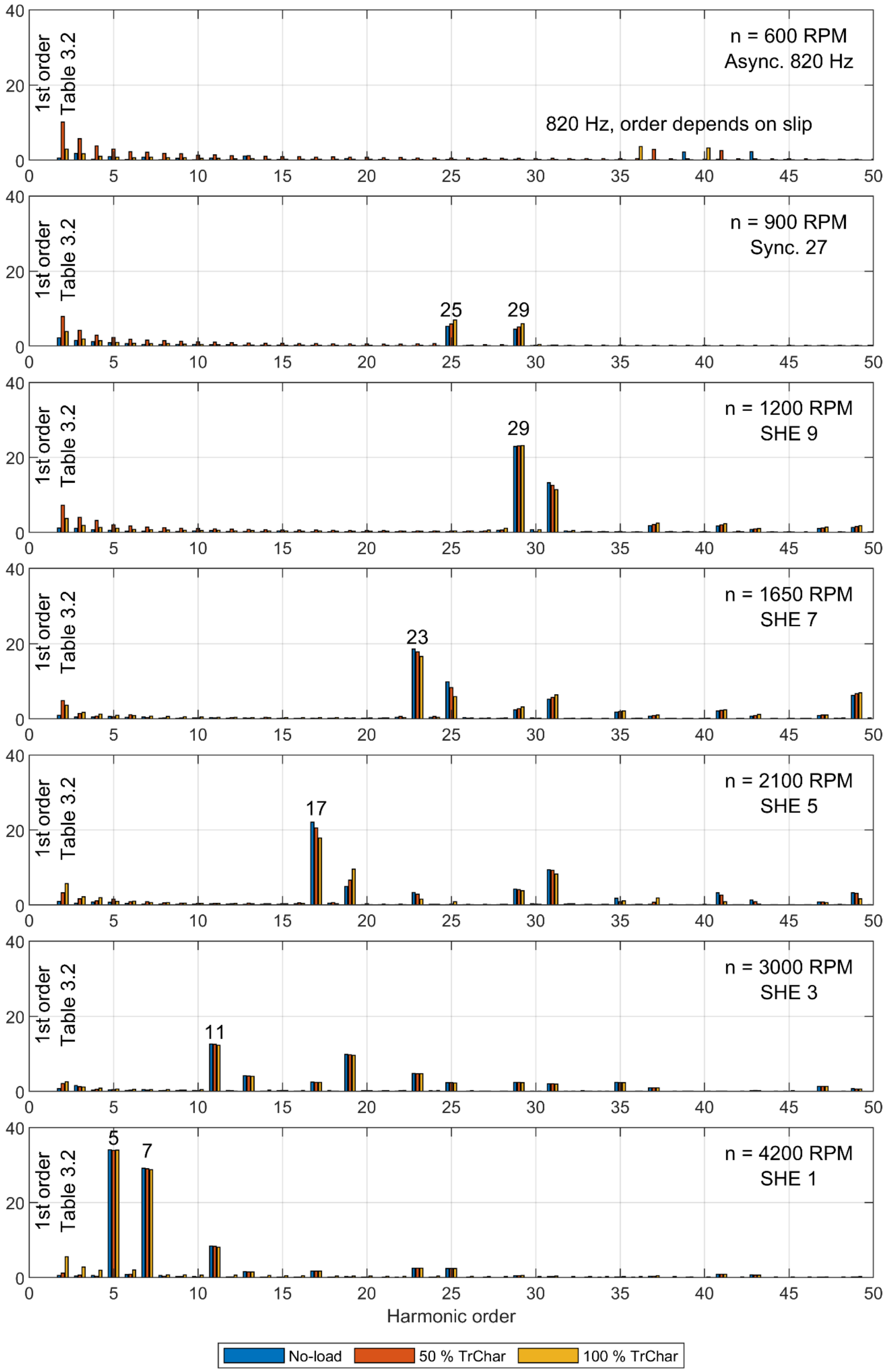

Fig. 3.2. FFT in each regime (excludes 1st harmonic).

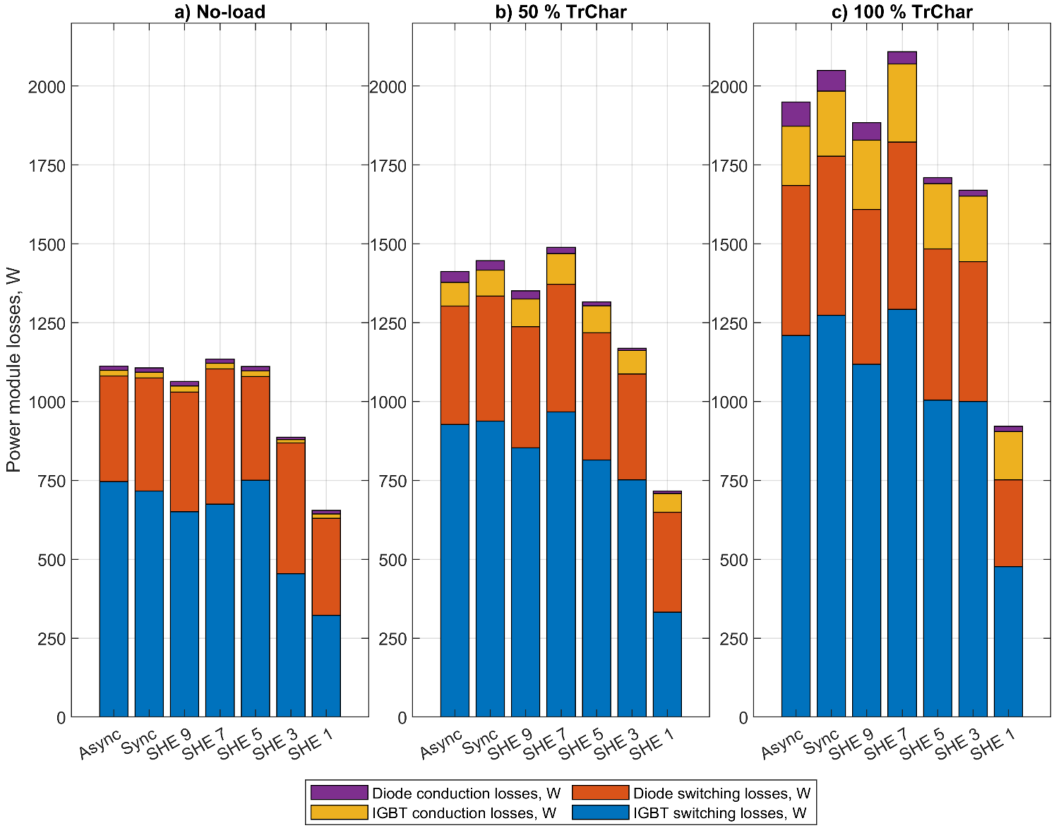

Fig. 3.3. Constituent losses of the power module.

Comparison of synchronous and SHE PWM

The next set of tests revolves around the comparison of the synchronous PWM and SHE PWM performance in different conditions. The test results are presented briefly with the main outcomes, while a full description is in the full text of the Thesis.

The first test was carried out at several reference points with synchronous PWM and SHE in different configurations. For this test, a manual PWM mode transition regime was set, which allows for an arbitrary pre-set combination of PWM modes with any setting to transition at any point in time.

Reference points are 900 RPM and 1140 RPM with 0 Nm, 1500 Nm and 3000 Nm loads representing 0 %, 50 % and 100 % of the reference traction characteristic in this area. At these speeds, three PWM pairs are tested with equivalent switching to fundamental frequency ratios of 23, 19, and 15 for synchronous and SHE PWM 11, 9, and 7, respectively.

It can be concluded that in THD, synchronous PWM is favourable because amplitudes of created harmonics are lower. However, WTHD is either close to SHE or lower in many cases, especially at higher loads and/or higher speeds. That is the case with WTHD because synchronous 23 has the main prominent harmonics at the 21st and 25th orders, synchronous 19 at the 17th and 21st, synchronous 15 at the 13th and 17th, while SHE 11 eliminates up to 34th and has boosted harmonics at the 35th and 37th orders, SHE 9 and SHE 7 have boosted at 29th/31st and 23rd/25th, respectively, which are significantly further than with synchronous PWM.

However, the assessment of losses presents a complex challenge. At no-load or under low-loading conditions, synchronous PWM provides lower power module losses (0.9–4 %) compared to the respective SHE. However, at 1500 Nm, the losses are either almost equal or SHE shows up to 3.4 % lower losses. At 3000 Nm, the losses are either nearly equal or SHE exhibits up to 7 % lower losses compared to synchronous PWM, depending on the m_f ratio.

It can be concluded that the lower the ratio of switching to fundamental frequency, the better the SHE performs. Additionally, at higher loads, SHE is more favourable due to both lower losses and lower WTHD. Further study on an adaptive transition scheme could investigate the combination of not only frequency-dependent but also load-dependent transition schemes, aiming to minimize both WTHD and losses.

Test 2 makes the comparison of synchronous and SHE PWM at the traction characteristic reference. During the modelling, instead of SHE 9, 7, 5, 3, and 1, synchronous PWM was selected with switching to fundamental frequency ratio of 19, 15, 11, 7, and 3, such that the switching frequency pattern stays consistent with original SHE PWM scheme Fig. 3.1. Operation with synchronous PWM with $m_f = 3$ was not stable and failed to reliably reach reference points.

It can be concluded that SHE 9/sync. 19 operate with very similar indicators, and it is inconclusive, which is more favourable. But it can be said that if the system does not go below m_f ratio of 19, standard synchronous PWM could be employed without almost any penalty. However, starting from SHE 7/sync. 15, THD/WTHD starts to increase with each transition quite significantly. SHE 5 and SHE 3 show the best results in terms of current quality at very low m_f ratios.

Starting at SHE 5/sync. 11, differences in THD/WTHD become very significant even under loaded conditions, making operation with synchronous PWM ill-advised. As is commonly stated in the literature, the minimum acceptable ratio of switching frequency to fundamental harmonic is typically 10, and the reasons for this are evident. The most prominent harmonics of sync. 7 are the 5th and 9th, whereas for SHE 3, they are the 11th and 13th. At sync. 7, compared to SHE 3, the RMS current becomes, on average, 4.4 % larger due to significantly elevated harmonics, even at full load. At no-load conditions, the difference is even more pronounced.

In conclusion, power module losses are, on average, 1.5 % lower with SHE than with synchronous PWM across all differing regimes (SHE 3, 5, 7, and 9). At SHE 5 and SHE 3, THD/WTHD is substantially lower than with the same frequency of synchronous PWM.

Comparison of different SHE solutions

SHE has multiple solutions depending on the number of notches per-quarter wave of the fundamental waveform. This research focuses more on the control system and general implementation of the hybrid PWM approach into the system and testing its stability. However, the test was conducted comparing different solutions for SHE 7 and SHE 9 utilizing each of the four unique solutions as proof of the actual numerical difference between solutions.

Table 3.3 outlines the reference points used in the test. In the PWM mode, a shortened value in brackets is used for further marking for conciseness.

Table 3.3

Overview of Reference Points

<table>
<tr><th rowspan="2">PWM mode</th><th rowspan="2">Reference speed, RPM</th><th colspan="6">Switching frequency, Hz | Modulation index</th></tr>
<tr><th colspan="2">No-load (A)</th><th colspan="2">1500 Nm (B)</th><th colspan="2">3000 Nm (C)</th></tr>
<tr><td>SHE 9, Solution 1 (9–1)</td><td rowspan="8">900</td><td rowspan="4">570</td><td rowspan="8">0.43</td><td rowspan="4">585</td><td rowspan="8">0.465</td><td rowspan="4">599</td><td rowspan="8">0.512</td></tr>
<tr><td>SHE 9, Solution 2 (9–2)</td></tr>
<tr><td>SHE 9, Solution 3 (9–3)</td></tr>
<tr><td>SHE 9, Solution 4 (9–4)</td></tr>
<tr><td>SHE 7, Solution 1 (7–1)</td><td rowspan="4">450</td><td rowspan="4">462</td><td rowspan="4">473</td></tr>
<tr><td>SHE 7, Solution 2 (7–2)</td></tr>
<tr><td>SHE 7, Solution 3 (7–3)</td></tr>
<tr><td>SHE 7, Solution 4 (7–4)</td></tr>
</table>

Table 3.4 summarizes results outlining stator current performance indicators. Table 3.4 has a red colour shading representing the maximum respective value and a light green colour representing the minimum respective value across solutions.

From the presented data it can be seen that there is no difference regarding the fundamental current component I_1 as it stays constant across the SHE types and its solutions, while different only depending on the load value. That is expected, as the task of the control system and the fundamental current hybrid observer is to keep the stator current's fundamental harmonic at a predefined level.

However, it is another story entirely when harmonic content and total losses are considered. Analyzing WTHD and stator current harmonic component, it can be seen that there is a measurable difference between solutions. In WTHD, the difference in SHE 9 is up to 45 %, and in SHE 7, it is up to 27 % , with the more prominent difference in no-load conditions, while at full load, the difference is up to 20 %. And when discussing $I_{2\dots50}$, differences between the worst- and best-case results can reach up to 19 %, while values remain relatively constant regardless of the load. Consequently, THD and WTHD decrease with increasing load.

Table 3.4

Summary of the Stator Current Indicators

Mode /n-ref	**THD, %**			**WTHD, %**			I_1			$I_{2\dots50}$		
	(A)	(B)	(C)	(A)	(B)	(C)	(A)	(B)	(C)	(A)	(B)	(C)
(9–1)	59.72	23.62	12.45	2.34	2.70	0.58	53.9	144.5	272.7	32.2	34.1	33.9
(9–2)	58.61	23.05	12.06	3.38	2.72	0.64	54.0	144.5	272.7	31.6	33.3	32.9
(9–3)	63.42	25.19	13.53	2.71	2.69	0.63	53.9	144.5	272.7	34.2	36.4	36.9
(9–4)	61.83	24.49	13.04	2.89	2.74	0.64	53.9	144.5	272.6	33.3	35.4	35.5
(7–1)	73.27	28.27	14.75	3.64	2.93	0.72	53.9	144.5	272.6	39.5	40.8	40.2
(7–2)	75.59	29.33	15.56	3.31	2.81	0.74	53.9	144.5	272.7	40.7	42.4	42.4
(7–3)	83.46	32.48	17.50	3.89	2.90	0.83	53.9	144.5	272.6	45.0	46.9	47.7
(7–4)	79.64	30.90	16.50	4.19	2.91	0.90	54.0	144.5	272.6	43.0	44.7	45.0

Regarding power module and, consequently, power converter losses, differences between solutions are measurable. Under no-load conditions, the maximum difference in losses is 2.5 %, while at full load, the maximum difference reaches 6 %. The most significant impact is due to the difference in IGBT switching loss because switching occurs at different phases of the current, and switching energy is mainly dependent on the instantaneous value of the current at the switching point.

In conclusion, there is a measurable difference between SHE solutions in both WTHD and power module losses. For the most efficient operation with the best achievable stator current quality, an optimization process should be developed at a later stage of development. However, the task of optimizing losses and WTHD falls outside the scope of the current research, and the preliminary results are presented as a basis for future research possibilities.

3.2. Control system performance without EMU

The next set of modelling tests outlines the control system performance without EMU. This way, it is possible to test the system's stability with higher rates of acceleration and with the application of static load.

The system is tested for flux response, speed response, and response to the disturbances (application of load torque). A summary of the main results is shown in the current subchapter.

Speed response

The speed response is tested without a rate limiter and with a 500 RPM/s^2 rate limiter from a standstill to maximum speed (4780 RPM) and back to a standstill. In the summary, visual results are shown for the test without limiter (see Fig. 3.4).

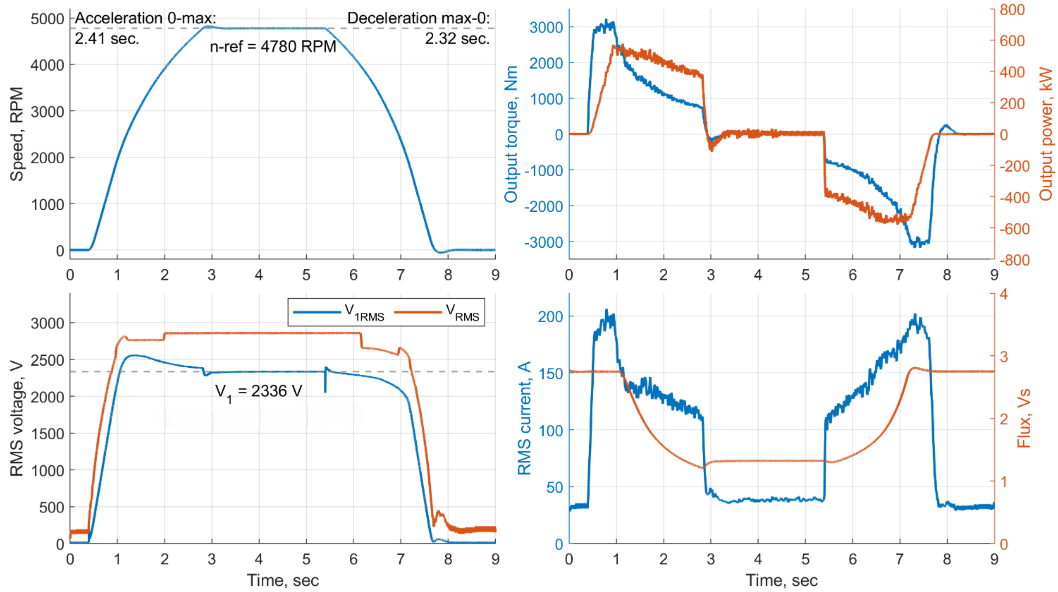

Fig. 3.4. Motor acceleration and deceleration at traction characteristic.

The test results performance indicators are summarized in Table 3.5.

Table 3.5

Summary of Performance Indicators

	TrChar limiter	**500 RPM/s^2 rate limiter**
Speed overshoot, acceleration	43.4 RPM / 0.9 % overshoot	23.7 RPM / 0.5 % overshoot
Speed overshoot, deceleration	–57.2 RPM	–25.4 RPM
Feedback-based voltage limiter	227 Vrms / 9.7 % overshoot	72.5 Vrms / 3.1 % overshoot
Acceleration time	2.41 seconds	9.56 seconds
Deceleration time	2.32 seconds	9.56 seconds

Even only with traction characteristics, the limiter system operates within the desirable performance. Both the control system and the fundamental current hybrid observer exhibit a much quicker response. While the maximum EMU acceleration is 0.95 m/s², which corresponds to

127 RPM/s², thus, the 500 RPM/s² rate limiter is four times quicker than the maximum train acceleration, providing more than enough capability for testing the control system dynamics.

Additionally, based on the described speed response test, the transition between modes and hybrid observer operation are analysed. From the results, it can be seen that modulation transitions happen smoothly even with the highest rate of acceleration achievable by the motor without the vehicle. Meaning that at slower rates transitions will not have any issues. At the same time, hybrid observer tracking is consistent and accurate even at a maximum acceleration rate. While at lower dynamics, tracking is even better.

Hybrid observer tracking was also tested at the harshest regime of SHE 3 and SHE 1 at no load, when harmonics are closest to the fundamental and are comparable in amplitude to the fundamental. Even with such a low switching frequency hybrid observer can track the fundamental waveform's phase and amplitude. However, it can be concluded that SHE 1 operation is extremely noisy, with harmonics exceeding the fundamental. Thus, the operation at no load, if possible, is not advisable, requiring an adaptive hybrid PWM transition scheme.

Reaction to load

The last test is the reaction of the system to the disturbance insertion, in this case, the loading of the motor with step torque at a specific speed. Three speed reference points with safety margins were considered for this test:

- 0 RPM, 900 Nm, asynchronous PWM $f_{sw} = 820\ Hz$
- 2140 RPM, 2184 Nm, SHE 5
- 4780 RPM, 673 Nm, SHE 1

A value lower than the traction characteristic limit at the corresponding speed is selected to provide a safety margin for the controller to react.

The numeric summary of the test results is presented in Table 3.6.

Table 3.6

Summary of the Performance Indicators

	Reference speed	0 RPM	2160 RPM	4780 RPM
	Reference torque	900 Nm	2184 Nm	673 Nm
	Voltage at no load	16 V	2190 V	2340 V
	Voltage at load	43 V	2340 V	2340 V
Load application	Max. speed / Δn	3.1 / 3.1	2173.2 / 13.2	4785.5 / 5.5
	Min. speed / Δn	–55.6 / –55.6	2035.1 / –124.9	4740.6 / –39.4
Load removal	Max. speed / Δn	54.1 / 54.1	2282.0 / 122	4819.4 / 39.4
	Min. speed / Δn	–3.1 / –3.1	2151.4 / –8.6	4777.6 / –2.4

From the results, it can be seen that the magnitude of the absolute error changes is based on the magnitude of the applied torque. In conclusion, it can be stated that the control system operates properly at defined speed reference points when applying external disturbance in a step manner.

3.3. Control system performance with EMU

The last test is the verification of the operation of the developed system with an EMU model. The test consists of 2 reference points:

- at 2 seconds, the speed reference is set to 120 km/h;
- at 80 seconds, the speed reference is set to 0 km/h.

This test checks how the system performs with the hybrid PWM and fundamental hybrid observer in maximum effort acceleration till maximum operating speed and then deceleration till the full stop. During both acceleration and deceleration, the system follows the pre-established transition pattern. Test results are summarized in two graphs shown in Fig. 3.5 and Fig. 3.6.

From the upper left section, it can be seen that the train takes 58.7 seconds to reach the maximum speed and 53 seconds to reach the full stop. During acceleration and deceleration, there is almost no overshoot.

The bottom left section of the graph presents the RMS voltage of the system. The red line represents the actual RMS stator line voltage, including all harmonics, while the blue line represents the fundamental component of the RMS stator line voltage. The fundamental component is limited to the 2340 VRMS voltage of the designed traction motor.

Upper right graphs clearly present output torque and power and outline the constant torque, constant power, and $1/v^2$ operation regions.

The bottom right graphs represent stator RMS current and system flux. The start of the field-wakening regime is visible.

It can be noted that the control system reliably reaches the provided speed reference and has an almost critically damped response with almost no overshoot (less than 0.1 %). The same could be said for the voltage. Before reaching the pre-defined fundamental RMS voltage limit, the system adheres to the V/f criterion and, after that, strictly follows the voltage limit without deviating from it.

Fig. *3.6* represents the constituent losses of the power module. All the transition points are clearly visible both in the rapid change of losses and by the markings with the dotted line. The hybrid PWM approach reliably limits losses in the power module below 2200 W in total. However, when reaching the speed reference, EMU goes into the regime of maintaining speed, which requires only a little tractive effort to combat the effects of train rolling resistance. At that point, the power module losses drop significantly, which opens a possibility for further optimization of the switching pattern, depending not only on frequency but also on load. That could be an area of further research.

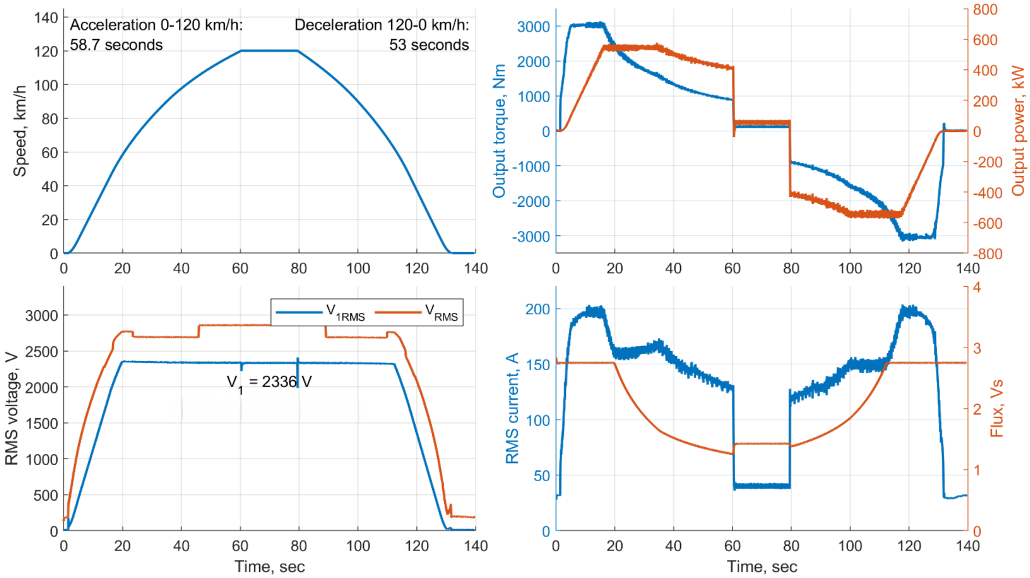

Fig. 3.5. EMU acceleration-deceleration – main performance indicators.

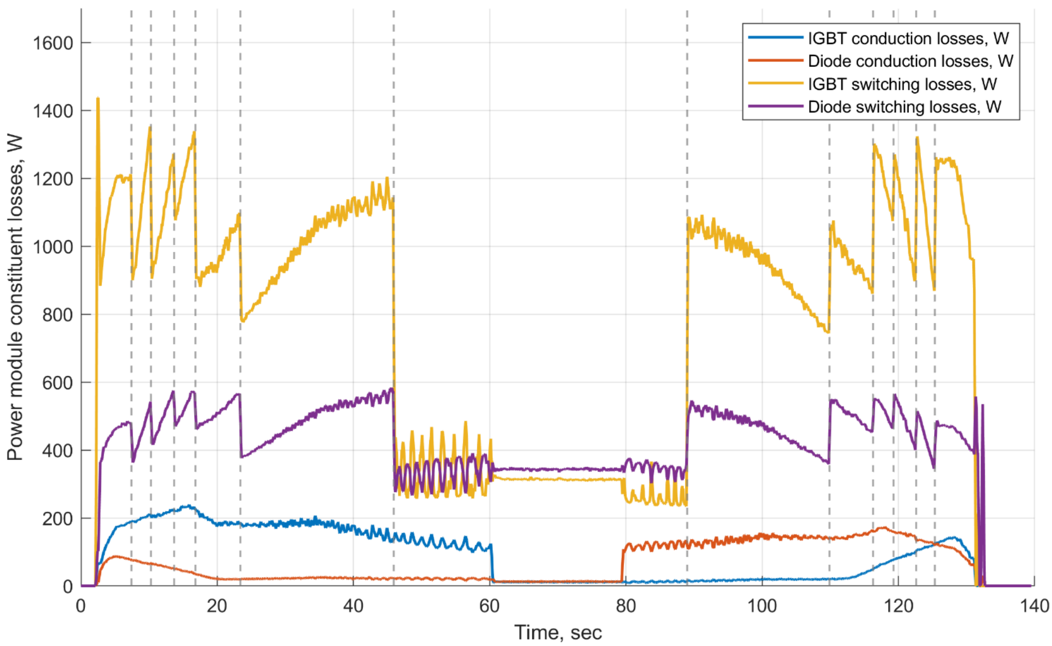

Fig. 3.6. Distribution of power module constituent losses.

4. Experimental Validation of the Developed Control System

Experimental validation of the actual setup is required once the system is stable in the model. However, when working with large and expensive electric drives, testing is conducted in steps, starting with a downscaled laboratory setup.

This research validates the developed system on a small, downscaled laboratory setup with adapted system limits and parameters. This chapter summarizes the laboratory setup and the necessary steps for transitioning from the parameters and limitations of the control system with EMU to the laboratory deployment. It is followed by a set of validation tests and an analysis of the results.

4.1. Description of the laboratory setup

This subchapter summarizes an overview of the setup with a description of select parts of the stand.

The developed control system is tested on a laboratory setup with a 2-level inverter. Experimental verification was conducted at the premises of Riga Technical University. A short description of the laboratory setup outlining each constituent part is as follows:

1. *Real-time simulator*: Opal-RT OP4510 (acts as a control board).
2. The industrial 2-level frequency inverter from Danfoss. The industrial inverter from Danfoss does not use the standard control board. Instead, it has a custom interface board allowing direct access to the control signals of the inverter: signal for each phase, inverter enable, and braking resistor signals while keeping overcurrent, overvoltage and overtemperature protection. In addition to that, the interface board includes dead-time management, preventing shoot-through of the transistors. The interface board accepts optical control signals.
3. Inverter for a load motor – SIEMENS AFE (Active Front-End) CU240S.
4. Test induction motor: ABB M2AA100LB-4 3GAA102002-ADE.
5. Load induction motor: Leroy Somer LS100L 380V 2.2kW. It is driven by the SIEMENS AFE inverter, equipped with a bidirectional rectifier bridge. This inverter is with a stock control system and is set in torque vector control mode. The stock control system is automatically tuned to the Leroy Somer motor based on the internal program of the Simens AFE inverter. The reference torque value is set from the OP4510 simulator.
6. Rotating torque meter: UTMII-20Nm. It measures output torque on the motor shaft and interconnects motors with backlash-free couplings.
7. Encoder: Scancon 2RHF2048-D-5M-S.

8. Current and voltage measurements box. Consists of LEM LA 55-P (3×) and LEM LV 25-600. Current sensors are installed on a custom PCB, which in turn, with a voltage sensor board, are assembled into a case.
9. DC-voltage power supply with 0–32 V range for supplying supplementary electronics.

OP4510 real-time simulator

OPAL-RT OP4510 is used as a control board for the main motor and for setting reference values of torque for the Siemens AFE, which drives the load motor. This setup is used for the initial stage of development as with Simulink and custom libraries from OPAL-RT control system deployment and testing takes considerably less time, compared to a custom-made control board.

Different signals act as inputs and outputs to and from OP4510. Below are the signals classified by their type:

1. Digital outputs produce five signals: three PWM signals of each inverter IGBT leg, enable and break resistor activation signals, which are fed to the Danfoss inverter. Signals go through a custom intermediary board. It converts the electrical digital outputs of the OP4510 to optical signals, which are sent to the input of the Danfoss inverter.
2. Analogue output is a single signal which is fed to the analogue input of the Siemens converter, which is set up to control output torque reference from 0 Nm to 15 Nm at 0 V to 10 V, respectively.
3. Analogue inputs are three current and one voltage measurement signal with a shunt resistor and a torque signal from a torque meter with a low pass filter based on the torque meter producer documentation.
4. The signal from the rotary encoder is read by an OPAL-RT RS422 differential encoder expansion board.

The developed control system is deployed using MATLAB with custom libraries from Opal-RT and RT-LAB software. In addition to that, a console is developed to set reference values and different miscellaneous parameters during online operation. The system deployed to OP4510 is set to run with a fixed step of 5 microseconds, with CPU utilization of 40–45 % and no overruns during extended run time periods.

On-demand data recording is set up with a high resolution of 50 kHz for a customizable short period of time and with a down-sampled resolution of 2 kHz for an extended amount of time.

4.2. Control system transition: from train to lab

An actual control system is being developed for the EMU implementation. However, the testing is carried out on a downscaled laboratory setup, thus necessitating adjustment of all control system parameters.

Induction motor parameters

The first step in the transition is the determination of the induction motor parameters and equivalent circuit, with downscaling of traction characteristics. The induction motor used for testing is ABB M2AA100LB-4 3GAA102002-ADE [61]. It is a 3-phase, 2-pole pair motor. The main parameters from the producer's datasheet for the continuous operation (S1) are shown in Table 4.1.

Table 4.1

S1 Working Point Parameters

Parameter name	Units	Value
Output power (on shaft)	kW	3
Stator voltage LL (V_{1rms})	V	380
Stator current	A	6.58
Power factor	-	0.85
Frequency	Hz	50
Slip	%	4.67
Rotational speed	RPM	1430
Mechanical torque	Nm	20
Maximum torque	Nm	58
Efficiency	%	85.0
Current, slip = 0	A	2.74

For the proper operation of the control system, an equivalent circuit of the test motor is necessary. Testing and equivalent circuit extraction are done in accordance with IEC 60034-28 standard. Table 4.2 summarises the results of equivalent circuit tests. Table 4.2 shows the nominal value of the magnetizing inductance at nominal flux and frequency, while the non-linear curve obtained is used in deployment.

Table 4.2

Equivalent Circuit Parameters

Parameter name	Units	Value
Stator resistance at 20 °C	mΩ	1817
Rotor resistance at 20 °C	mΩ	1478
Magnetizing inductance	mH	230
Leakage inductance ($L_{\sigma s} = L_{\sigma r}$)	mH	9.5
Inertia of the rotor	kgm^2	0.022
Viscous friction coefficient	Nms/rd	0.002

Controller coefficients

Following updated motor parameters, control system coefficients are recalculated. Recalculated PI controller coefficients and respective parameters are shown in Table 4.3.

Table 4.3

Summary of the Controller Coefficients

Controller	$\boldsymbol{T_i}$	$\boldsymbol{k_i = \frac{k_p}{T_i}}$	$\boldsymbol{k_p}$	**Rise time**	**Settling time**	**Overshoot**
d-/q- current	4.1 ms	1488	6.1	4.3 ms	12.5 ms	4.9 %
Speed	94.3 ms	5.0	0.47	50.3 ms	313 ms	22.8 %
Flux	45.5 ms	250	11.4	46.4 ms	215 ms	13.7 %
Field-weakening	45.5 ms	16.3	0.74			

Traction limiting characteristic

Traction limiting characteristic is adjusted based on the motor capabilities and on the loading capabilities of the coupled motor and its inverter. The output torque limit is reduced proportionally to the traction characteristic of the large traction motor. It is downscaled based on torque in a constant torque region from 3000 Nm to 20 Nm by a factor of 150. Transition points between regimes 1)–2) and 2)–3) are kept the same for consistency, while the transition point between 3)–4) is changed according to the 15A instantaneous current limit of the frequency converter.

Additionally, the maximum speed is reduced to 120 Hz, or approximately 3450–3600 RPM depending on the slip. The loading inverter is locked to 120 Hz of maximum fundamental frequency, and mechanical coupling and mechanical alignment have been designed for speeds only up to 4000 RPM.

Traction characteristic has the following regions:

1. 0–350 RPM: gradual increase of torque from 6.7 Nm to 20 Nm. It is kept to be consistent with a large traction motor.
2. 350–1720 RPM: constant torque region limited by $T_{out} = 20$ Nm.
3. 1720–2600 RPM: constant power region limited by $P_{out} = 3.6$ kW.
4. 2600–3600 RPM (max speed): $T_{elm}\omega_m \cong constant$ or $T_{em} \propto \frac{1}{\omega_s^2}$ region.

The load torque limit is 75 % of the control system limits as the inverter is limited to 15 Nm to give a safety margin for the control system not to go into saturation. In addition, many tests are carried out at 50 % of the load torque limit.

PWM transition scheme

All tests have identical hybrid PWM transition types and points of transition. Parameters of each PWM modulation mode are shown in Fig. 4.1 showing the hybrid PWM transitions scheme in visual form. Used in laboratory testing, the transition scheme is mostly identical to the one used during modelling, with the only difference being that the SHE 3 to SHE 1 transition point is shifted down, so it is in the speed range.

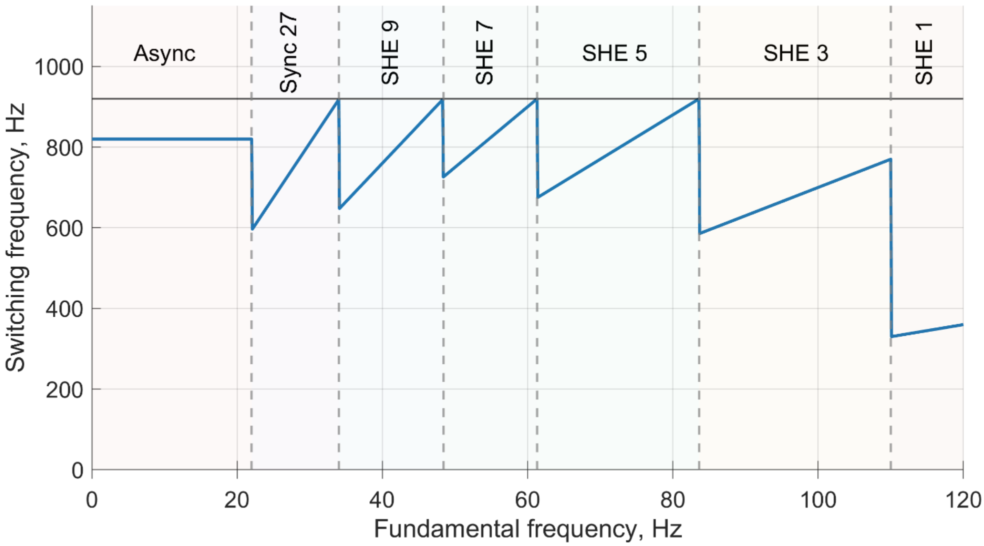

Fig. 4.1. Hybrid PWM transitions scheme (used in laboratory).

4.3. Analysis of stator current harmonic content and motor losses

This subchapter summarizes the harmonic analysis of the induction motor stator current and induction motor losses during static operation. Modelling addresses losses in the power module, while laboratory tests allow for direct measurement of motor losses and efficiency. However, converter losses cannot be measured directly.

Several tests were carried out to depict the THD, WTHD, and converter losses while outlining the differences between modulation modes. The sets of tests are designed to be as close as possible to the modelling ones. Speeds are maintained at predefined levels with reference torques scaled down. All calculations and data post-processing are performed in the same way as in the modelling phase.

Overview of modulation performance in static regime

The first test is an overview of PWM in each mode. Table 4.4 provides an overview of used reference points, where TrChar is the load limit reference.

Table 4.4

Overview of Reference Points

PWM mode	**Reference speed, RPM**	**Reference torque, Nm | Switching frequency, Hz**					
		No-load (A)		0.5 TrChar (B)		TrChar (C)	
Asynchronous (1)	600	0	820	7.5	820	15	820
Synchronous 27 (2)	900	0	812	7.5	834	15	858
SHE 9 (3)	1200	0	762	7.5	778	15	794
SHE 7 (4)	1650	0	827	7.5	841	15	860
SHE 5 (5)	2100	0	772	6.14	786	12.28	805
SHE 3 (6)	3000	0	702	3.72	714	7.45	733
SHE 1 (7)	3450	0	346	2.82	351	5.63	360

Table 4.5 provides the stator current performance indicators, with Fig. 4.2 providing harmonic values at integer harmonic orders in relation to the fundamental frequency. Fig. 4.2 excludes the 1st harmonic as it is significantly different between no-load and fully loaded regime.

Table 4.5

Summary of the Stator Current Indicators

Mode / Load	**THD, %**			**WTHD, %**			I_1			$I_{2\dots50}$		
	(A)	(B)	(C)	(A)	(B)	(C)	(A)	(B)	(C)	(A)	(B)	(C)
(1)	11.44	10.64	8.82	1.78	2.30	2.09	3.46	4.82	7.41	0.40	0.51	0.65
(2)	22.21	17.61	13.56	2.21	2.00	1.86	3.49	4.92	7.50	0.77	0.87	1.02
(3)	42.94	29.81	20.14	2.94	2.14	2.03	3.51	4.99	7.60	1.51	1.49	1.53
(4)	29.85	20.67	12.89	3.51	2.78	1.63	3.41	5.03	8.31	1.02	1.04	1.07
(5)	48.70	26.59	15.71	6.10	3.53	2.44	2.54	4.72	8.42	1.23	1.25	1.32
(6)	55.29	24.82	13.37	11.03	5.11	2.95	1.84	4.15	8.04	1.02	1.03	1.08
(7)	155.55	72.57	38.94	33.25	15.79	8.57	1.77	3.79	7.26	2.76	2.75	2.83

It can be seen that each regime on the laboratory setup works as intended, with expected harmonics appearing in each regime.

Asynchronous PWM, as expected, has harmonics at $f_{sw} - 2 \cdot f_0$, $f_{sw} + 2 \cdot f_0$, $2 \cdot f_{sw} - f_0$, $2 \cdot f_{sw} + f_0$ etc [62], which corresponds at no-load to 780, 860, 1620, and 1660 Hz, respectively, and harmonic order of 39th, 43rd, 81st, and 83rd.

Synchronous PWM with the ratio of $m_f = 27$ has the most prominent harmonics at $m_f \pm 2$ and at $2 \cdot m_f \pm 1$ [62], which is 25th, 29th, 53rd and 55th harmonics, respectively.

Selective harmonic elimination has expected harmonics eliminated with next odd non-triplen boosted harmonics annotated in Fig. 4.2.

It can be seen that SHE 1 has poor harmonic performance, especially at no-load, where it is only the case when harmonic current is higher than fundamental. As was noted previously, SHE 1 and/or square wave modulation should be avoided if possible. However, the control system is able to accurately track the speed of the motor at no-load and loaded conditions, even in SHE 1.

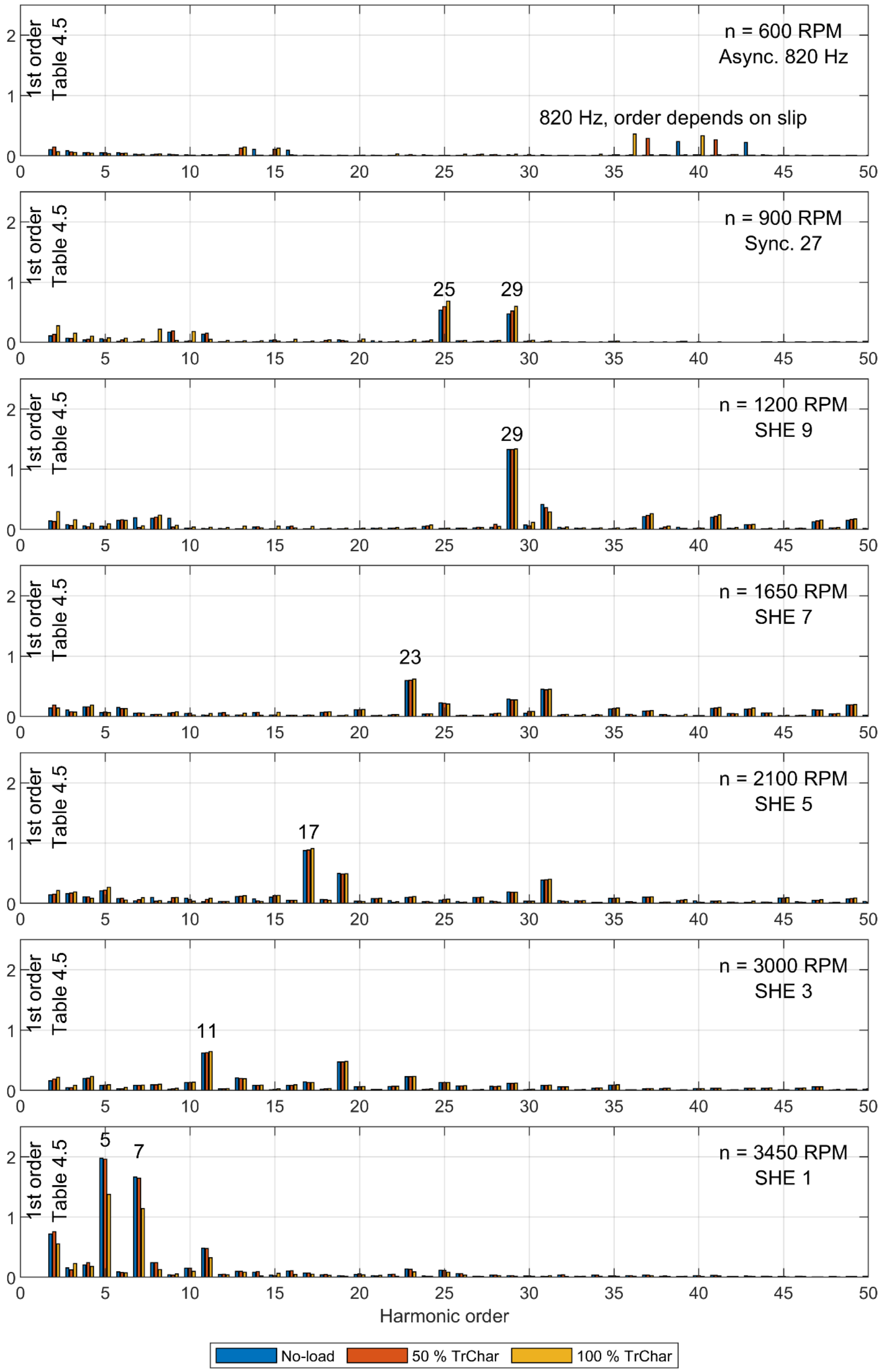

Fig. 4.2. FFT in each regime (excludes the 1st harmonic).

Comparison of synchronous and SHE PWM

The following set of tests revolves around the comparison of the synchronous PWM and SHE PWM performance in different conditions.

The first test is done with synchronous and SHE PWM at the same switching frequency. This test outlines the difference between synchronous and SHE PWM. In this test, pairs of synchronous and SHE PWM were analysed and tested for current THD/WTHD as well as for motor losses, which are measured directly with the help of a torque transducer.

It can be concluded based on the results that at lower m_f ratios, both WTHD and motor losses are substantially lower, while at higher speeds and/or higher m_f ratios, WTHD is comparable. Combining modelling results and laboratory measurements, it can be concluded that SHE, compared with the synchronous PWM at the same switching frequency, provides comparable results at the no-load condition, while lower power module and motor losses at loaded conditions.

The second test is done with synchronous and SHE PWM at traction characteristic reference. This subchapter summarizes the comparison of operation with mode transition scheme utilizing SHE and synchronous PWM with the same switching frequency. Instead of SHE 9, 7, 5, 3, and 1, synchronous PWM was selected with switching to a fundamental frequency ratio of 19, 15, 11, 7, and 3, such that the switching frequency pattern stays consistent with the original SHE PWM scheme.

The first thing should be noted that the system with synchronous PWM was tested up to 3300 RPM, up to the transition to the ratio of 3, because the system was unstable and could not operate with the m_f ratio of 3, while with SHE 1 the system was operational, however having very high THD.

Based on the test results it can be concluded that SHE 9/sync. 19 results are comparable. However, the higher speed / lower m_f ratio clearly shows the comparative advantage of the SHE, as both losses and THD/WTHD are superior compared to the synchronous, as well as the system being stable and operational at SHE 1.

Maximum motor loss difference is 98 W at 2700 RPM or up to 15 %.

- In the 3rd phase, SHE, on average, has 6 % higher losses.
- In the 4th phase, SHE, on average, has 2 % lower losses.
- In the 5th–6th phase, SHE, on average, has 10 % lower losses.

At the same time, in all phases, synchronous PMW has higher THD and higher WTHD.

It can be concluded that below $m_f = 19$, it is advisable to use pre-programmed PWM as in this case SHE-PWM. These results show that both THD/WTHD and motor losses are superior, while modelled power module losses show slight benefit in the use of SHE with no detriment.

Comparison of different SHE solution

Table 4.6

Overview of Reference Points

PWM mode	Reference speed, RPM	Switching frequency, Hz | Modulation index					
		No-load (A)		7.5 Nm (B)		15 Nm (C)	
SHE 9, Solution 1 (9–1)	900	572	0.608	588	0.645	605	0.689
SHE 9, Solution 2 (9–2)							
SHE 9, Solution 3 (9–3)							
SHE 9, Solution 4 (9–4)							
SHE 7, Solution 1 (7–1)		451		464		477	
SHE 7, Solution 2 (7–2)							
SHE 7, Solution 3 (7–3)							
SHE 7, Solution 4 (7–4)							

Table 4.7

Summary of the Stator Current Indicators

Mode / n-ref	*THD*, %			*WTHD*, %			I_1			$I_{2...50}$		
	(A)	(B)	(C)	(A)	(B)	(C)	(A)	(B)	(C)	(A)	(B)	(C)
(9–1)	60.19	44.30	30.86	2.90	2.33	2.48	3.51	4.92	7.48	2.12	2.18	2.31
(9–2)	57.55	42.13	29.21	2.88	2.26	2.42	3.51	4.92	7.49	2.02	2.07	2.19
(9–3)	66.69	49.50	34.73	3.52	2.66	2.61	3.53	4.93	7.48	2.35	2.44	2.60
(9–4)	63.69	47.04	32.89	3.11	2.51	2.49	3.51	4.93	7.49	2.24	2.32	2.46
(7–1)	68.80	50.03	34.63	3.60	2.70	2.70	3.51	4.93	7.50	2.42	2.47	2.60
(7–2)	73.84	54.16	37.67	3.69	2.78	2.76	3.52	4.93	7.50	2.60	2.67	2.82
(7–3)	84.04	61.83	43.25	4.42	3.16	2.99	3.53	4.95	7.50	2.97	3.06	3.24
(7–4)	78.48	57.59	40.14	4.07	2.94	2.85	3.52	4.94	7.50	2.77	2.85	3.01

Table 4.8

Summary of the Motor Power Indicators

Mode / n-ref	P_{in}, W			P_{out}, W			P_{loss}, W			η, %		
	(A)	(B)	(C)	(A)	(B)	(C)	(A)	(B)	(C)	(A)	(B)	(C)
(9–1)	117	869	1734	47	729	1409	70.3	139.9	324.8	40.0	83.9	81.3
(9–2)	118	868	1734	47	730	1409	71.2	138.9	325.2	39.7	84.0	81.3
(9–3)	129	880	1749	47	730	1409	82.1	150.2	340.0	36.3	82.9	80.6
(9–4)	125	876	1741	47	730	1409	78.3	146.1	331.9	37.5	83.3	80.9
(7–1)	138	890	1756	48	731	1411	90.5	159.2	345.2	34.6	82.1	80.3
(7–2)	144	896	1767	48	731	1411	96.3	165.0	355.9	33.1	81.6	79.9
(7–3)	166	921	1793	48	731	1410	117.8	190.1	382.6	28.9	79.4	78.7
(7–4)	156	909	1778	48	731	1410	108.1	178.0	367.6	30.7	80.4	79.3

The next test is the comparison of SHE solutions. A single point at 900 RPM is measured under four sets of solutions at three loading conditions. An overview of reference points is shown in Table 4.6. Results are presented in the same way as in previous subchapters with current performance indicators in Table 4.7 and motor power indicators in Table 4.8.

It can be seen that there is a substantial difference in WTHD and total power loss with different SHE solutions. WTHD has the lowest WTHD/motor losses with SHE 9–2 and SHE 7–1 and the highest with SHE 9–3 and 7–3 and differences ranging from 8 % to 20 %, while motor losses change in accordance with WTHD. Lower the WTHD and lower the losses of the motor, with the difference in losses ranging from 5 % to 30 %.

Based on modelling and testing results, it can be concluded that each SHE solution has slightly different performance in regard to WTHD, power module losses, and motor losses. Due to that, it is possible to optimize WTHD and losses in traction operation for EMU both in acceleration-deceleration (under load) and in maintaining speed (low load).

4.4. Control system performance

The next set of laboratory tests is done to evaluate the control system's performance with the developed control system. The set of tests is done in the same way or closely resembling the ones in the modelling section.

Speed response

This test outlines the response of the system to the change in reference speed. Two sets of tests were carried out:

1. Acceleration 0–3600 RPM (n max) with the only limiter being traction characteristic. Only acceleration is tested for as at rapid deceleration even with used braking resistor DC-link voltage rises significantly with very fast ramp or no-limiter. Therefore, it was decided to exclude this test for the safety of equipment. In addition, the hybrid observer struggles with very fast dynamics, as is shown further.
2. Acceleration and deceleration 0–3600 RPM (n max) – 0 RPM with 500 RPM/s^2 rate limiter. Results are shown in Fig. 4.3.

Performance indicators of the test results are summarised in Table 4.9.

It can be seen that the system is stable and successfully reaches the reference speed with both ramps while also smoothly transitioning between regimes of modulation, following a pre-defined transition scheme.

Acceleration time is substantially faster at the traction characteristic limit (0.81 seconds instead of 2.41 seconds) due to the substantial inertia difference of 360 times (8 kgm^2 and 0.022 kgm^2), while the traction characteristic ratio between large and small motors is 150 times. In addition, the reference speed is 3600 RPM instead of 4780 RPM in the model.

While for the 500/s^2 limited acceleration/deceleration speed overshoot is the same, and voltage overshoot is slightly lower.

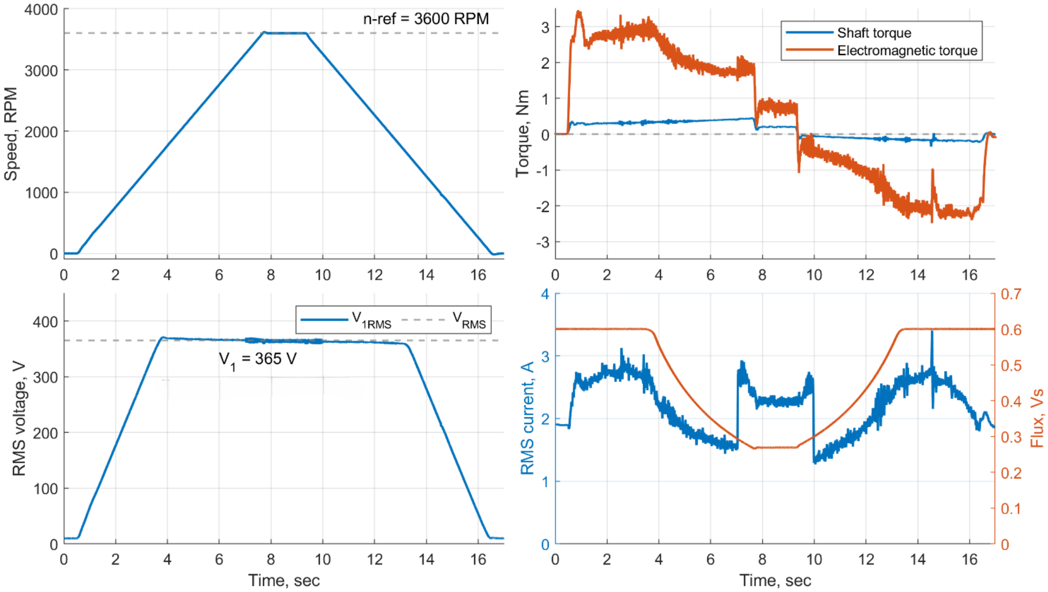

Fig. 4.3. Motor acceleration and deceleration at 500 RPM/s^2 ramp.

Table 4.9

Summary of Performance Indicators

	TrChar rate limiter	500 RPM/s^2 rate limiter
Speed overshoot, acceleration	130 RPM / 3.6% overshoot	17.7 RPM / 0.5% overshoot
Speed overshoot, deceleration	-	–9 RPM
Feedback-based voltage limiter 365 Vrms limit	40 Vrms / 11.0 % overshoot	6 Vrms / 1.6 % overshoot
Acceleration time	0.81 seconds ≈ 4400 RPM/s^2	7.2 seconds
Deceleration time	-	7.2 seconds

Additionally, based on the speed response test transition between modes and hybrid observer operation are analysed. It can be concluded that the modulation transitions happen smoothly even with high rates of acceleration, while hybrid observer results slightly differ from the simulation stage.

From hybrid observer operation, it can be concluded that with 500/s^2, rate tracking is accurate in a dynamic regime. However, at the traction characteristic limit, which amounts to approximately

4400 RPM/s^2 acceleration, the observer struggles to accurately track the stator current. That shows that there is a practical limit on the performance of the observer. For this implementation, this dynamic is more than enough as 500 RPM/s^2 is already 4 times faster than the fastest acceleration of the train under consideration.

In the simulation stage, an additional test was conducted at 3000 RPM with SHE 3 and at 3450 RPM with SHE 1 in no-load conditions to outline the observer tracking in the most challenging regimes. Based on the results, it can be stated that the observer successfully tracks the fundamental current, even at SHE 1. However, with SHE 1, it is difficult to state visually as harmonics exceed the value of fundamental, and there is even harmonic at such a low m_f ratio. However, FFT analysis shows that the amplitude of the actual and tracked fundamental harmonics is equal.

Reaction to load

The last test is the reaction of the system to the disturbance-loading of the motor. The following points are selected:

- 0 RPM, 5 Nm, asynchronous PWM $f_{sw} = 820$ Hz (reaction at standstill);
- 1500 RPM, 15 Nm reference, SHE 7 (reaction at speed near the voltage limit at no-load);
- 3600 RPM, 5.17 Nm, SHE 1 (point at maximum speed).

Table 4.10 summarizes the results of the test and additionally provides measured mechanical and electromagnetic torque. It can be seen that the reference and actual torque differ slightly due to the error margin of the loading inverter.

Table 4.10

Summary of the Performance Indicators

	Reference speed	0 RPM	1500 RPM	3600 RPM
	Reference torque	5 Nm	15 Nm	5.17 Nm
	Measured mechanical torque	4.56 Nm	15.37 Nm	5.41 Nm
	Electro-magnetic torque, Nm	5.82 Nm	16.08 Nm	6.69 Nm
	Electromagnetic torque limit, Nm	6.7 Nm	20 Nm	6.9 Nm
	Voltage at no-load	10 V	339 V	364 V
	Voltage at load	14.7 V	364 V	364 V
Load application	Max. speed / Δn	2.3 / 2.3	1532.2 / 32.2	3606 / 6
	Min. speed / Δn	–63.6 / -63.6	1326.1 / –173.9	3508.5 / –91.5
Load removal	Max. speed / Δn	70.3 / 70.3	1675.2 / 175.2	3693.1 / 93.1
	Min. speed / Δn	–1 / –1	1461.9 / 38.1	3594.9 / 5.1

In conclusion, it can be stated that the control system operates properly at defined speed reference points when applying external disturbance in a step manner.

Conclusions

Due to the characteristics of power modules used in power converters of high-power medium voltage electric drives for railway applications, they are limited to switching frequencies of usually no more than 1 kHz, therefore necessitating a special hybrid pulse-width modulation (PWM) approach.

The developed hybrid PWM approach consists of conventional asynchronous and synchronous PWM and pre-programmed PWM – in the case of this research, it is selective harmonic elimination (SHE) PWM. Due to the inherent properties of the SHE PWM, it requires some version of the fundamental current estimator to reliably operate with a field-oriented control (FOC) system.

This research details a step-by-step methodology for the creation and validation of a traction drive control system specifically designed for railway applications with low switching frequency.

During the development process, an in-depth exploration of the hybrid PWM approach was conducted, encompassing its integration into the control system. This involved extensive research, algorithmic formulation, implementation on the control board, and subsequent evaluation on a downscaled laboratory setup.

The developed control system was initially simulated in Simulink, where it went through extensive testing and finetuning before being deployed into a real-time machine OPAL-RT OP4510 acting as a control board for downscaled laboratory setup. The subsequent phase involved the adaptation of all coefficients and limitations onto the laboratory setup with a set of similar tests to the model phase.

The following key conclusions can be drawn based on the research:

1) The optimized Newton–Raphson algorithm for solving SHE and selective harmonic mitigation (SHM) problems for 2-/3-level inverters demonstrates faster convergence and reduced computational effort compared to standard solvers. Such computational improvements are especially important for higher-order harmonics, complex solution spaces, iterative minimizations in cases of SHM and advanced optimization tasks.
2) FOC system utilizing hybrid observer and hybrid PWM transition scheme tested at the low switching frequency, limited to a maximum of 920 Hz, with an average of 735 Hz, exhibits stable performance.
3) Hybrid observer provides stable and accurate tracking with at least 500 RPM/s^2 acceleration and at no-load with lowest m_f ratios.
4) SHE provides lower measured motor losses – up to 16 %, with an average of 8 %, as well as lower calculated power module losses – up to 7 %, with an average of 1 %. These

results, however, are highly dependent on the load compared to an equivalent switching frequency with synchronous PWM for SHE 1, 3, 5, and 7. SHE 9 and 11 provide similar results to synchronous PWM, as the harmonics are far enough from the fundamental frequency to have a significant effect.

5) Many SHE stages have several unique sets of solutions. Each solution at the same modulation index eliminates the same harmonics while providing different WTHD and losses. Experimental testing has shown that motor losses vary by up to 30 %, with an average of 15 %, while simulations have indicated that power module losses vary by up to 6 %, with an average of 2.9 % between best and worst-performing SHE solutions. While these findings indicate that certain SHE solutions are more effective under specific conditions, this study does not establish a single universally optimal SHE solution set for a real EMU. The most suitable choice would likely depend on the particular operational profile, design constraints, and performance targets of the specific EMU application.

In summary, as initially hypothesized, the traction drive control system with the FOC system can reliably operate at low switching frequencies while staying within power converter loss limitations to avoid exceeding junction temperatures.

Additionally, it was established that SHE has a substantial advantage over synchronous PWM with the same equivalent frequency in terms of WTHD, power module losses, and motor losses. These differences are especially prominent at low switching-to-fundamental frequency ratios and under loaded conditions.

However, at high m_f ratios, the advantages of SHE diminish, making synchronous PWM easier to use. Moreover, at high numbers of eliminated harmonics, there are many unique solutions and angle calculations become a time-consuming process. The most significant effects of SHE were found with SHE 3, 5, and 7, with SHE 9 also being considered. However, with a higher number of switches, the advantages of SHE become negligible in this application, or synchronous PWM performs better, especially at low or no load.

The main novelty of this research is the development of a methodology for the creation, tuning, and testing of the traction drive FOC system with a hybrid PWM. Additionally, the research includes the development of an optimized Newton–Raphson method for solving the SHE/SHM problem for 2-/3-level inverters.

Future research could be extended to the following areas:

- Development of the selection criteria for transition points specific to power module/motor configurations.
- Optimization of the hybrid PWM transition scheme based not only on frequency but also on output torque.
- Selection of specific SHE solutions to further optimize WTHD, power module and motor losses.
- Emulation of EMU operation in a laboratory setup, as demonstrated by P. Fajri, V. Prabhala, and M. Ferdowsi in 2016 [63].

List of References

[1] 'Motor Catalogue', Alstom, Feb. 2015.

[2] 'Rail Vehicles | TSA – Traktionssysteme Austria', TSA. Accessed: Apr. 05, 2024. [Online]. Available: https://www.tsa.at/rail/

[3] 'Traction systems for locomotives and high-speed applications', ABB, 2018. Accessed: Jan. 26, 2024. [Online]. Available: https://library.e.abb.com/public/896cf517fcce4406b7a4facb6d6b7d0c/Traction_systems_high%20power_RevB_180916_web.pdf

[4] G. Abad, Ed., *Power electronics and electric drives for traction applications*. Chichester, West Sussex, United Kingdom: Wiley, 2017.

[5] 'BORDLINE® CC750 DC_1500V For regional trains (EMU) with 1500 Vdc grid voltage', ABB, Product data sheet, Feb. 2020. Accessed: Apr. 05, 2024. [Online]. Available: https://search.abb.com/library/Download.aspx?DocumentID=3BHS262330%20ZAB%2005&LanguageCode=en&DocumentPartId=&Action=Launch

[6] M. Adamowicz and J. Szewczyk, 'SiC-Based Power Electronic Traction Transformer (PETT) for 3 kV DC Rail Traction', *Energies*, vol. 13, no. 21, Art. no. 21, Jan. 2020, doi: 10.3390/en13215573.

[7] 'EMU ELF2 Project Data Sheet.', Ingeteam, Jul. 2017. Accessed: Apr. 05, 2024. [Online]. Available: https://www.ingeteam.com/Portals/0/Catalogo/Sector/Documento/SSE_2793_Archivo_ref-t15-elf2-emu.pdf

[8] I. T. AG, 'Silicon Carbide (SiC) – Infineon Technologies'. Accessed: Apr. 05, 2024. [Online]. Available: https://www.infineon.com/cms/en/product/technology/silicon-carbide-sic/

[9] 'Silicon Carbide (SiC) Power Modules | Semikron Danfoss'. Accessed: Apr. 05, 2024. [Online]. Available: https://www.semikron-danfoss.com/innovation-technology/silicon-carbide-power-modules.html

[10] 'CoolSiC(TM) General presentation Part 2 – Why SiC from Infineon?', Infineon, Mar. 2024. Accessed: Apr. 08, 2024. [Online]. Available: https://www.infineon.com/cms/en/product/power/mosfet/silicon-carbide/

[11] C. S. Goli, S. Essakiappan, P. Sahu, M. Manjrekar, and N. Shah, 'Review of Recent Trends in Design of Traction Inverters for Electric Vehicle Applications', in *2021 IEEE 12th International Symposium on Power Electronics for Distributed Generation Systems (PEDG)*, Jun. 2021, pp. 1–6. doi: 10.1109/PEDG51384.2021.9494164.

[12] E. Robles, A. Matallana, I. Aretxabaleta, J. Andreu, M. Fernández, and J. L. Martín, 'The role of power device technology in the electric vehicle powertrain', *International Journal of Energy Research*, vol. 46, no. 15, pp. 22222–22265, 2022, doi: 10.1002/er.8581.

[13] Yole Development, 'Power SiC 2022', Product Brochure, 2022. Accessed: Apr. 05, 2024. [Online]. Available: https://medias.yolegroup.com/uploads/2022/03/Power-SiC-2022-Product_Brochure.pdf

[14] L. Diao, J. Tang, P. C. Loh, S. Yin, L. Wang, and Z. Liu, 'An Efficient DSP–FPGA-Based Implementation of Hybrid PWM for Electric Rail Traction Induction Motor Control', *IEEE Transactions on Power Electronics*, vol. 33, no. 4, pp. 3276–3288, Apr. 2018, doi: 10.1109/TPEL.2017.2707639.

[15] T. Jing, A. Maklakov, A. Radionov, V. Gasiyarov, and Y. Liang, ‘Formulations, Solving Algorithms, Existing Problems and Future Challenges of Pre-Programmed PWM Techniques for High-Power AFE Converters: A Comprehensive Review’, *Energies*, vol. 15, no. 5, Art. no. 5, Jan. 2022, doi: 10.3390/en15051696.

[16] J. Napoles, J. I. Leon, R. Portillo, L. G. Franquelo, and M. A. Aguirre, ‘Selective Harmonic Mitigation Technique for High-Power Converters’, *IEEE Transactions on Industrial Electronics*, vol. 57, no. 7, pp. 2315–2323, Jul. 2010, doi: 10.1109/TIE.2009.2026759.

[17] G. Nalcaci, D. Yildirim, I. Cadirci, and M. Ermis, ‘Selective Harmonic Elimination for Variable Frequency Traction Motor Drives Using Harris Hawks Optimization’, *IEEE Transactions on Industry Applications*, vol. 58, no. 4, pp. 4778–4791, Jul. 2022, doi: 10.1109/TIA.2022.3174828.

[18] ‘BORDLINE® CC750 MS (1 kVDC and 11 kVAC/16.7 Hz) Propulsion and auxiliary converter for dual-voltage multiple unit trains’, ABB, Product data sheet, 2012. Accessed: Apr. 05, 2024. [Online]. Available: https://library.e.abb.com/public/1219655d9aadccd7c1257a040063b32c/PDS%20BORDLINE%20CC750%20MS_3BHS262330%20ZAB%20E09%20Rev%20A.pdf

[19] J. Chivite-Zabalza, M. A. Rodríguez Vidal, P. Izurza-Moreno, G. Calvo, and D. Madariaga, ‘A Large Power, Low-Switching-Frequency Voltage Source Converter for FACTS Applications With Low Effects on the Transmission Line’, *IEEE Transactions on Power Electronics*, vol. 27, no. 12, pp. 4868–4879, Dec. 2012, doi: 10.1109/TPEL.2012.2192753.

[20] Janusz Biliński, Sylwester Buta, Emil Gmurczyk, and Jerzy Kaska, ‘Nowoczesny asynchroniczny napęd z hamowaniem odzyskowym produkcji MEDCOM do zmodernizowanych elektrycznych zespołów trakcyjnych serii EN57AKŁ’, MEDCOM, Apr. 2012. Accessed: Apr. 22, 2024. [Online]. Available: https://yadda.icm.edu.pl/baztech/element/bwmeta1.element.baztech-article-BPK6-0021-0081/c/Bilinski.pdf

[21] ‘BORDLINE® CC750 AC_15-25kV For regional trains (EMUs) with 15/25 kVac line voltage’, ABB, Product data sheet, Mar. 2018. Accessed: Apr. 05, 2024. [Online]. Available: https://library.e.abb.com/public/2a3a5170c8ed4550a661a6b1533ce968/BORDLINE%20CC750%20AC_15-25kV_M_700%20RevC%20EN.pdf

[22] A. Hughes, *Electric motors and drives: fundamentals, types, and applications*, Fourth Edition. Amsterdam: Elsevier/Newnes, 2013.

[23] H. Li and K. W. Klontz, ‘An investigation of current harmonic influence on induction motor in hybrid electric vehicle application’, in *2017 IEEE International Electric Machines and Drives Conference (IEMDC)*, May 2017, pp. 1–6. doi: 10.1109/IEMDC.2017.8002201.

[24] J. I. Leon, S. Kouro, L. G. Franquelo, J. Rodriguez, and B. Wu, ‘The Essential Role and the Continuous Evolution of Modulation Techniques for Voltage-Source Inverters in the Past, Present, and Future Power Electronics’, *IEEE Transactions on Industrial Electronics*, vol. 63, no. 5, pp. 2688–2701, May 2016, doi: 10.1109/TIE.2016.2519321.

[25] M. Steczek, P. Chudzik, and A. Szeląg, ‘Combination of SHE- and SHM-PWM Techniques for VSI DC-Link Current Harmonics Control in Railway Applications’, *IEEE Transactions on Industrial Electronics*, vol. 64, no. 10, pp. 7666–7678, Oct. 2017, doi: 10.1109/TIE.2017.2694357.

[26] J. Holtz and N. Oikonomou, ‘Estimation of the Fundamental Current in Low-Switching-Frequency High Dynamic Medium-Voltage Drives’, *IEEE Transactions on Industry Applications*, vol. 44, no. 5, pp. 1597–1605, Sep. 2008, doi: 10.1109/TIA.2008.2002212.

[27] N. Mohan, T. M. Undeland, and W. P. Robbins, *Power electronics: converters, applications and design*, 3rd ed. Hoboken, NJ: John Wiley & Sons, 2003.

[28] D. G. Holmes and T. A. Lipo, *Pulse width modulation for power converters: principles and practice*. Hoboken, NJ: John Wiley, 2003.

[29] J.-S. Yim, S.-K. Sul, B.-H. Bae, N. R. Patel, and S. Hiti, 'Modified Current Control Schemes for High-Performance Permanent-Magnet AC Drives With Low Sampling to Operating Frequency Ratio', *IEEE Transactions on Industry Applications*, vol. 45, no. 2, pp. 763–771, Mar. 2009, doi: 10.1109/TIA.2009.2013600.

[30] R. P. Aguilera *et al.*, 'Closed-loop SHE-PWM technique for power converters through Model Predictive Control', in *IECON 2015 – 41st Annual Conference of the IEEE Industrial Electronics Society*, Nov. 2015, pp. 005261–005266. doi: 10.1109/IECON.2015.7392928.

[31] L. G. Franquelo, J. Napoles, R. C. P. Guisado, J. I. Leon, and M. A. Aguirre, 'A Flexible Selective Harmonic Mitigation Technique to Meet Grid Codes in Three-Level PWM Converters', *IEEE Transactions on Industrial Electronics*, vol. 54, no. 6, pp. 3022–3029, Dec. 2007, doi: 10.1109/TIE.2007.907045.

[32] D. Chatterjee, A. Szeląg, and M. Steczek, 'Analysis of disturbing effect of 3 kV DC supplied traction vehicles equipped with two-level and three-level VSI on railway signalling track circuits', *Bulletin of the Polish Academy of Sciences: Technical Sciences; 2017; 65; No 5 (Special Section on Multilevel Converters); 663–674*, 2017, Accessed: Apr. 05, 2024. [Online]. Available: https://journals.pan.pl/dlibra/publication/121389/edition/105775

[33] J. E. Huber and A. J. Korn, 'Optimized Pulse Pattern modulation for Modular Multilevel Converter high-speed drive', in *2012 15th International Power Electronics and Motion Control Conference (EPE/PEMC)*, Sep. 2012, pp. LS1a-1.4-1-LS1a-1.4-7. doi: 10.1109/EPEPEMC.2012.6397383.

[34] T. Geyer and N. Oikonomou, 'Model predictive pulse pattern control with very fast transient responses', in *2014 IEEE Energy Conversion Congress and Exposition (ECCE)*, Sep. 2014, pp. 5518–5524. doi: 10.1109/ECCE.2014.6954157.

[35] V. Spudic, T. Geyer, and N. Oikonomou, 'Optimized Pulse Patterns for Mmc Control', EP3142236A1, Mar. 15, 2017

[36] H. S. Patel and R. G. Hoft, 'Generalized Techniques of Harmonic Elimination and Voltage Control in Thyristor Inverters: Part I–Harmonic Elimination', *IEEE Transactions on Industry Applications*, vol. IA-9, no. 3, pp. 310–317, May 1973, doi: 10.1109/TIA.1973.349908.

[37] H. S. Patel and R. G. Hoft, 'Generalized Techniques of Harmonic Elimination and Voltage Control in Thyristor Inverters: Part II – Voltage Control Techniques', *IEEE Transactions on Industry Applications*, vol. IA-10, no. 5, pp. 666–673, Sep. 1974, doi: 10.1109/TIA.1974.349239.

[38] A. M. Hava, R. J. Kerkman, and T. A. Lipo, 'A high-performance generalized discontinuous PWM algorithm', *IEEE Transactions on Industry Applications*, vol. 34, no. 5, pp. 1059–1071, Sep. 1998, doi: 10.1109/28.720446.

[39] I. M. Alsofyani and K.-B. Lee, 'Simple Capacitor Voltage Balancing for Three-Level NPC Inverter Using Discontinuous PWM Method With Hysteresis Neutral-Point Error Band', *IEEE Transactions on Power Electronics*, vol. 36, no. 11, pp. 12490–12503, Nov. 2021, doi: 10.1109/TPEL.2021.3074957.

[40] H. Khan, ‘Optimised space vector modulation for variable speed drives’, phdthesis, Université Blaise Pascal – Clermont-Ferrand II, 2012. Accessed: Dec. 16, 2022. [Online]. Available: https://theses.hal.science/tel-00999475

[41] H. Neudorfer, ‘Elektrische Bahnen Teil 1, Theorie’, Technische Universität Darmstadt, Mar. 2021. Accessed: Apr. 26, 2024. [Online]. Available: https://www.ew.tu-darmstadt.de/media/ew/rd/ew_vorlesungen/lv_bahnen/Skript_EB_2021.pdf

[42] ‘Europe rail electrification map’. Accessed: Apr. 29, 2024. [Online]. Available: https://commons.wikimedia.org/wiki/File:Europe_rail_electrification_en.svg

[43] *IEC 60034-28:2012 Rotating electrical machines – Part 28: Test methods for determining quantities of equivalent circuit diagrams for three-phase low-voltage cage induction motors*, International Standard 60034–28, Dec. 13, 2012. Accessed: Apr. 25, 2024. [Online]. Available: https://webstore.iec.ch/publication/133

[44] F. Giri, Ed., *AC electric motors control: advanced design techniques and applications*. Chichester, West Sussex, United Kingdom: John Wiley & Sons Inc, 2013.

[45] A. Sciarretta and A. Vahidi, *Energy-Efficient Driving of Road Vehicles: Toward Cooperative, Connected, and Automated Mobility*. in Lecture Notes in Intelligent Transportation and Infrastructure. Cham: Springer International Publishing, 2020. doi: 10.1007/978-3-030-24127-8.

[46] V. Burenin, ‘Research and Development of Electrical Drive Control System for Electrical Vehicle in Urban Environment’, Master Thesis, Riga Technical University, 2020.

[47] В. Е. Розенфельд, *Теория электрической тяги*, 3rd ed. Москва: Транспорт, 1995.

[48] T. Ogawa, S. Manabe, G. Yoshikawa, Y. Imamura, and M. Kageyama, ‘Method of Calculating Running Resistance by the Use of the Train Data Collection Device’, *Quarterly Report of RTRI*, vol. 58, no. 1, pp. 21–27, 2017, doi: 10.2219/rtriqr.58.1_21.

[49] A. Wintrich, U. Nicolai, W. Tursky, and T. Reimann, *Application manual power semiconductors*, 2nd revised edition. Ilmenau: ISLE Verlag, 2015.

[50] ‘5SNA 0600G650100’. Nov. 2015. Accessed: Jun. 21, 2024. [Online]. Available: https://search.abb.com/library/Download.aspx?DocumentID=5SYA1558-04&LanguageCode=en&DocumentPartId=&Action=Launch

[51] ‘ABB Library – 5SNA 0600G650100_IGBT_XML’. Accessed: Jun. 21, 2024. [Online]. Available: https://library.abb.com/d/5SNA%200600G650100_IGBT_XML

[52] ‘ABB Library – 5SNA 0600G650100_Diode_XML’. Accessed: Jun. 21, 2024. [Online]. Available: https://library.abb.com/d/5SNA%200600G650100_Diode_XML

[53] J. Holtz, ‘Pulsewidth modulation for electronic power conversion’, *Proceedings of the IEEE*, vol. 82, no. 8, pp. 1194–1214, Aug. 1994, doi: 10.1109/5.301684.

[54] A. Birda, J. Reuss, and C. M. Hackl, ‘Simple Fundamental Current Estimation and Smooth Transition Between Synchronous Optimal PWM and Asynchronous SVM’, *IEEE Transactions on Industrial Electronics*, vol. 67, no. 8, pp. 6354–6364, Aug. 2020, doi: 10.1109/TIE.2019.2938490.

[55] B. Akin and M. Bhardwaj, ‘Sensored Field Oriented Control of 3-Phase Induction Motors’. Texas Instruments Incorporated, 2013.

[56] B. K. Bose, *Modern power electronics and AC drives*. Upper Saddle River, NJ: Prentice Hall, 2002.

[57] R. S. Burns, *Advanced control engineering*. Oxford ; Boston: Butterworth-Heinemann, 2001.

[58] T. Pérez Soriano and J. Fernández Martínez, 'Low Speed Open Loop Field Oriented Control for Permanent Magnet Machines', Master Thesis, Aalborg University, 2011. [Online]. Available: https://kbdk-aub.primo.exlibrisgroup.com/discovery/fulldisplay?docid=alma9921564406405762&context=L&vid=45KBDK_AUB:DDPB&lang=en&search_scope=Projekter&adaptor=Local%20Search%20Engine&tab=ProjekterSpecialer&query=any,contains,3954a0f4-9734-484d-b587-be63843b9840&offset=0

[59] M. P. Kaźmierkowski, R. Krishnan, and F. Blaabjerg, Eds., *Control in power electronics: selected problems*. In Academic Press series in engineering. Amsterdam ; New York: Academic Press, 2002.

[60] *IEC 61000-4-7:2002 Electromagnetic compatibility (EMC) – Part 4–7: Testing and measurement techniques – General guide on harmonics and interharmonics measurements and instrumentation, for power supply systems and equipment connected thereto*, 2002. Accessed: Jan. 13, 2023. [Online]. Available: https://webstore.iec.ch/publication/4226

[61] ABB, 'Drive Low Voltage General Purpose Motors: Aluminium motor section'. ABB, Sep. 2003. Accessed: Jul. 18, 2024. [Online]. Available: https://library.e.abb.com/public/2652441d9397714dc1257b1300571151/General%20Purpose%20Motors%20Aluminium%20GB%20092003.pdf

[62] S.-H. Kim, *Electric motor control: DC, AC, and BLDC motors*. 2017.

[63] P. Fajri, V. A. K. Prabhala, and M. Ferdowsi, 'Emulating On-Road Operating Conditions for Electric-Drive Propulsion Systems', *IEEE Transactions on Energy Conversion*, vol. 31, no. 1, pp. 1–11, Mar. 2016, doi: 10.1109/TEC.2015.2481180.

Vsevolod Burenin was born in 1996 in Pskov, Russia. He received a degree of Bachelor of Engineering (2018) and a degree of Master of Engineering (2020) in Electrical Engineering from Riga Technical University, Riga, Latvia. Since 2019, he has been employed as a software engineer in the Department of Power Electronics at JSC "Riga Electrical Machinery Factory". His research interests include the design, control, and testing of electrical motors and traction drives.